Volume 12 | Number 9 | 7 May 2025

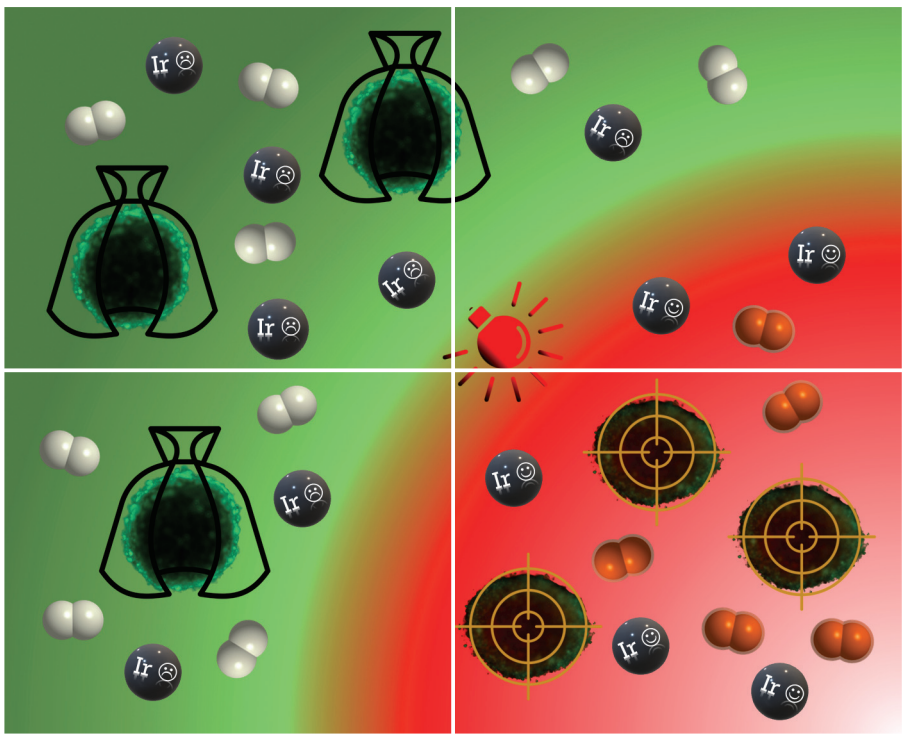

INORGANIC CHEMISTRY

FRONTIERS

CCS 中国化学会 CHINESE CHEMICAL SOCIETY

PEKING UNIVERSITY 1898

ROYAL SOCIETY OF CHEMISTRY

rsc.li/frontiers-inorganic

INORGANIC CHEMISTRY FRONTIERS

RESEARCH ARTICLE

View Article Online
View Journal | View Issue

Cite this: *Inorg. Chem. Front.*, 2025, **12**, 3367

Achieving red-light anticancer photodynamic therapy under hypoxia using Ir(III)–COUPY conjugates†

Enrique Ortega-Forte, [a,c] Anna Rovira,[b] Pezhman Ashoo, [a] Eduardo Izquierdo-García, [b] Cormac Hally,[c] Diego Abad-Montero, [b] Mireia Jordà-Redondo,[c] Gloria Vigueras, [a] Alba Deyà,[d] José Luis Hernández,[d] Jorge Galino,[d] Manel Bosch,[e] Marta E. Alberto, [f] Antonio Francés-Monerris, [g] Santi Nonell, [c] José Ruiz *[a] and Vicente Marchán *[b]

Despite the potential of photodynamic therapy (PDT), this oxygen-dependent oncological treatment is greatly restricted in the clinic by the well-known hypoxic feature of solid tumors. Here we provide new insights into the development of PDT agents based on conjugates between COUPY fluorophores and cyclometalated iridium(III) complexes with the aim of overcoming this limitation. The structural modifications carried out within the metal core of Ir(III)–COUPY conjugates, based on the incorporation of trifluorobenzyl groups at the cyclometalating ligands, enabled efficient exploitation of type I PDT mechanisms while retaining operativity under long-wavelength visible light, which facilitated deeper tissue penetration compared with short wavelengths. Photobiological evaluation revealed that Ir(III)–COUPY conjugate **3c** achieved potent photocytotoxicity towards cisplatin-resistant ovarian (A2780cis) and mammary (EO771) cancer cell lines, efficiently photogenerated type I and type II ROS, and photoinduced apoptotic cell death using red light irradiation (620 nm). Importantly, this Ir(III)–COUPY conjugate retained such potent photoactivity under low-oxygen environment conditions (2% O_2), delivering equipotent photocytotoxicity towards normoxic and hypoxic adherent cancer cells. Compound **3c** was found to be highly phototoxic against EO771 multicellular tumor spheroids and showed no signs of toxicity or adverse effects in mice, which could facilitate *in vivo* phototherapeutic applications. Taken together, this study demonstrates that the conjugation between COUPY dyes and rationally designed Ir(III) complexes is a strategy at the frontier of the development of new red light-activated photosensitizers capable of operating under hypoxia, showing the promise of achieving satisfactory anticancer PDT effects.

Received 31st December 2024,
Accepted 4th March 2025

DOI: 10.1039/d4qi03369h

rsc.li/frontiers-inorganic

Introduction

Photodynamic therapy (PDT) is a clinically approved form of cancer treatment in which a light-activated drug, commonly referred to as photosensitizer (PS), and molecular oxygen are involved in the process of tumor cell killing.[1–3] Many PSs have been developed in different chemical platforms, including porphyrins, chlorins, organic fluorophores and diverse nanosystems and biomaterials.[4–9] Recently, transition metal complexes emerged as promising systems for anticancer PDT, with Ru(II)- and Ir(III)-based PSs leading to early-stage preclinical and clinical applications.[10–18] However, despite these achievements, two major challenges posed by the chemical properties of current commercial PS drugs limit the efficacy of PDT: (1) photoactivation at long wavelengths *i.e.*, red or near-infrared (NIR) light, and (2) photoactivity retention under low concentrations of oxygen (hypoxia), conditions inevitably encountered

[a]*Departamento de Química Inorgánica, Universidad de Murcia, Biomedical Research Institute of Murcia (IMIB-Arrixaca), E-30100 Murcia, Spain. E-mail: jruiz@um.es*
[b]*Departament de Química Inorgànica i Orgànica, Secció de Química Orgànica, Universitat de Barcelona (UB), Institut de Biomedicina de la Universitat de Barcelona (IBUB), Martí i Franquès 1-11, E-08028 Barcelona, Spain. E-mail: vmarchan@ub.edu*
[c]*Institut Químic de Sarrià, Universitat Ramon Llull, Vía Augusta 390, E-08017 Barcelona, Spain*
[d]*Health and Biomedicine Department, Leitat Technological Center, Carrer de la Innovació 2, E-08225 Terrassa, Spain*
[e]*Unitat de Microscòpia Òptica Avançada, Centres Científics i Tecnològics, Universitat de Barcelona, Av. Diagonal 643, E-08028 Barcelona, Spain*
[f]*Dipartimento di Chimica e Tecnologie Chimiche, Università della Calabria, Arcavacata di Rende I-87036, Italy*
[g]*Institut de Ciència Molecular, Universitat de València, P.O. Box 22085, València 46071, Spain*

† Electronic supplementary information (ESI) available. See DOI: https://doi.org/10.1039/d4qi03369h

in growing solid tumors. Overcoming the former challenge, which limits the reachable penetration depth of PDT in biological tissues, has been attempted, for example, by using strategies that integrate or conjugate metal complexes with low-molecular weight organic fluorophores to red-shift the absorption of the PS to the phototherapeutic window. Examples of this include cyclometalated Ru(II) and Ir(III) complexes conjugated to boron-dipyrromethene (BODIPY),[19,20] porphyrin,[21] xanthene,[22] and rhodamine derivatives.[23] The hypoxia limitation, however, is more difficult to tackle since most PSs operate *via* the type II PDT mechanism, which relies on the presence of oxygen to produce highly toxic singlet oxygen ($^1O_2$).[24–26] In view of this limitation, we succeeded in developing type I PDT agents based on the conjugation of cyclometalated Ir(III) complexes to coumarin–pyridine (COUPY) fluorophores, which are less oxygen-sensitive and exhibit potent photoactivity upon blue or green light irradiation.[27,28] A structure–activity relationship study further revealed key structural modifications to the coumarin scaffold that improved the hypoxia performance of the Ir(III)–COUPY PSs.[29] Recently, we also disclosed a method to red-shift the operability of a cyclometalated Ru(II) polypyridyl system towards the NIR region through the conjugation of a COUPY fluorophore with operativity in the phototherapeutic window.[30]

Photoactivation *via* low-energy wavelength irradiation is more difficult to achieve for single Ir(III)-based systems bearing polypyridyl ligands since their absorption tail typically lies within the blue region of the electromagnetic spectrum.[13,31] Yet the development of cyclometalated cationic Ir(III)-based PDT agents is highly desirable because they generally possess larger Stokes' shifts and longer luminescence lifetimes, which add bioimaging capacity to the PDT effects.[32–36] We therefore envisioned new PSs based on Ir(III)–COUPY conjugates in which modifications of the cyclometalated Ir complex coupled to a far-red/NIR-emitting COUPY fluorophore could both defeat hypoxic environments and enable photoactivation at long wavelengths.

With this idea in mind, herein we explored the photobiological properties of two PSs based on the conjugation of COUPY dyes **1a** and **1b** to Ir(III) complex **2a** (compounds **3a** and **3b**, respectively; Fig. 1) upon 620 nm light irradiation, and reported a new Ir(III)–COUPY PS (**3c**) bearing trifluorobenzyl groups at the cyclometalating ligand of the metal complex (**2b**). The incorporation of trifluorobenzyl groups was made with the aim of exploiting type I PDT mechanisms, since some Ir(III) complexes containing these groups were reported to be superoxide radical generators under hypoxic conditions.[32]

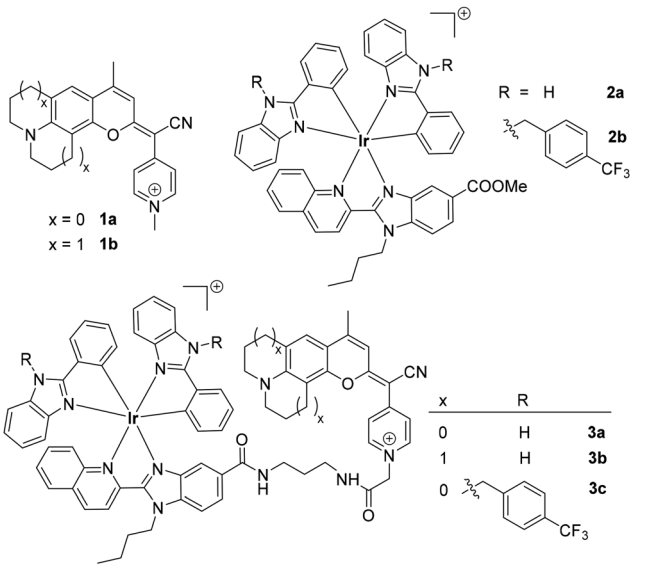

Fig. 1 Structure of the compounds investigated in this work: COUPY coumarins **1a** and **1b**, cyclometalated Ir(III) complexes **2a** and **2b**, and the corresponding Ir(III)–COUPY conjugates **3a–3c**.

Results and discussion

Synthesis and characterization

The Ir(III) complexes **2a** and **2b** and conjugates **3a** and **3b** were prepared as previously reported.[27,29,37] The Ir(III)–COUPY conjugate **3c** (Fig. 1) was synthesized by following our previously described methodology, which was based on the formation of an amide bond between the primary amino group of a suitable coumarin derivative and the carboxylic acid group of the required conjugatable Ir(III) complex **4** (Schemes S1 and S2†). The compounds were purified by column chromatography on silica gel and fully characterized by NMR spectroscopy and HRMS.

Photophysical and photochemical characterization

The photophysical and photochemical properties [absorption and emission spectra, molar absorption coefficients (ε), fluorescence (Φ_F) or phosphorescence (Φ_P) quantum yields, fluorescence (τ_F) or phosphorescent (τ_P) lifetimes, and singlet oxygen quantum yield (Φ_Δ)] were studied for the newly synthesized Ir(III)–COUPY conjugate (**3c**) and the parent Ir(III) complex (**2b**) in three solvents of different polarities (PBS, ACN and DCM), and compared with those of the previously reported conjugates (**3a** and **3b**) and the non-conjugated parent compounds (**1a**, **1b** and **2a**) (Fig. 2a, Fig. S5 and S6, and Tables S1 and S2†).[29] As expected, the Ir(III)–COUPY conjugate **3c** displayed similar absorption and emission maxima to those of **3a**, since both PSs share the same coumarin (*e.g.* in ACN, λ_{abs} = 556 nm and λ_{em} = 606 nm for **3c** *vs.* λ_{abs} = 555 nm and λ_{em} = 615 nm for **3a**). In contrast, conjugate **3b** bearing the julolidine-fused system in the coumarin moiety showed the largest red-shift in the absorption and emission maxima (*e.g.* in ACN, λ_{abs} = 580 nm and λ_{em} = 647 nm). Notably, the new Ir(III)–COUPY conjugate **3c** showed higher values of molar absorption coefficients in all the solvents studied and a higher luminescent quantum yield, especially in organic solvents (*e.g.* in ACN, Φ_P = 0.08 for **3a** and **3b** *vs.* Φ_P = 0.43 for **3c**). In PBS, both the coumarins and, especially, the Ir(III)–COUPY conjugates, showed aggregation, as revealed by the lower absorption

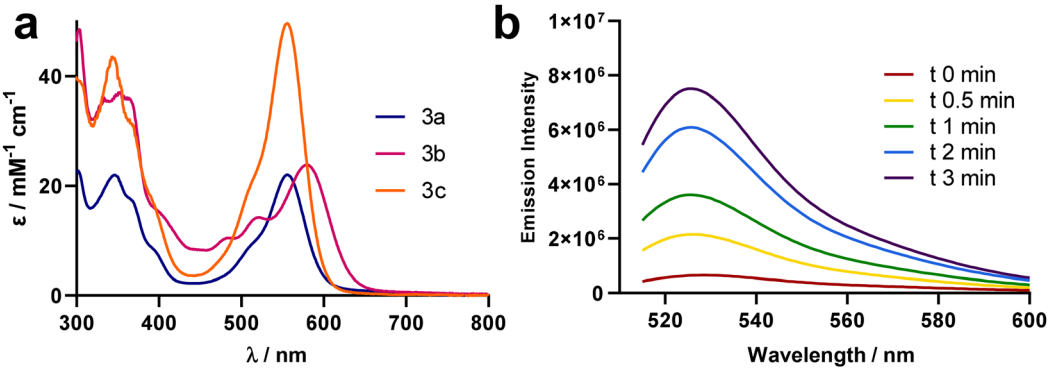

Fig. 2 (a) Comparison of the absorption spectra of Ir(III)–COUPY conjugates **3a–3c** in ACN. For other solvents, please see Fig. S5 and S6.† (b) Fluorescence spectra of ROS probe DHR123 in PBS induced by irradiation with red light (620 ± 15 nm; 130 mW cm^{-2}) in the presence of **3c**.

coefficients, broadening of the absorption bands, and decrease in the fluorescence quantum yields.

Singlet oxygen quantum yields (Φ_Δ) were determined by direct observation of the $^1O_2$ phosphorescence (λ_{exc} = 355 or 532 nm). As shown in Table S1,† the Ir(III) complex **2b** shows similar $^1O_2$ quantum yields to those of **2a** in all solvents. However, conjugation of the Ir(III) complex **2b** with the COUPY fluorophore **1a**, a very poor $^1O_2$ photosensitizer, resulted in an increase of the $^1O_2$ quantum yield of the Ir(III)–COUPY conjugate **3c** in all organic solvents (Table S2†), which reproduced the previously observed trends with conjugates **3a** and **3b**, leading to comparable quantum yields for all three Ir(III)–COUPY PSs in organic solvents. In PBS, the production of $^1O_2$ was negligible for all compounds.

Given the capability of **3a** and **3b** to generate the superoxide anion radical ($O_2^{\bullet-}$) within cells upon exposure to green light,[27,29] we focused on investigating if these Ir(III)–COUPY conjugates, along with the newly synthesized **3c**, could produce this specific type-I ROS under red light irradiation in PBS. To our delight, the use of the fluorogenic probe dihydrorhodamine 123 (DHR123) showed that all of them were capable of generating $O_2^{\bullet-}$ under red light irradiation (620 nm), contrasting with the behavior of the parent Ir(III) complexes (**2a** and **2b**) and COUPY derivatives (**1a** and **1b**) alone, which did not produce significant $O_2^{\bullet-}$ under the same irradiation conditions (Fig. 2b and Fig. S7†). Notably, the enhancement of the DHR123 fluorescence signal by the different Ir(III)–COUPY conjugates could be prevented using the $O_2^{\bullet-}$-specific scavenger tiron (Fig. S8 and S9†).

The generation of type I and type II ROS by conjugates **3a** and **3c** was also evidenced by electron paramagnetic resonance (EPR). The spin traps 4-amino-2,2,6,6-tetramethylpiperidine (4-amino-TEMP) and 5,5-dimethyl-1-pyrroline-*N*-oxide (DMPO) were used to detect $^1O_2$ and $O_2^{\bullet-}$, respectively. As shown in Fig. 3a, while no EPR signal was observed in the dark, the triplet signal characteristic of the TEMPO spin adduct (peak integral ratio 1 : 1 : 1) appeared upon irradiation with green light, confirming that compound **3a**, and even more so compound **3c**, could effectively photogenerate $^1O_2$. Furthermore, the detection of the four distinctive peaks of the DMPO-$O_2^{\bullet-}$ adduct (peak integral ratio 1 : 1 : 1 : 1) upon irradiation with green light also confirmed the ability of compounds **3a** and **3c** to produce super-

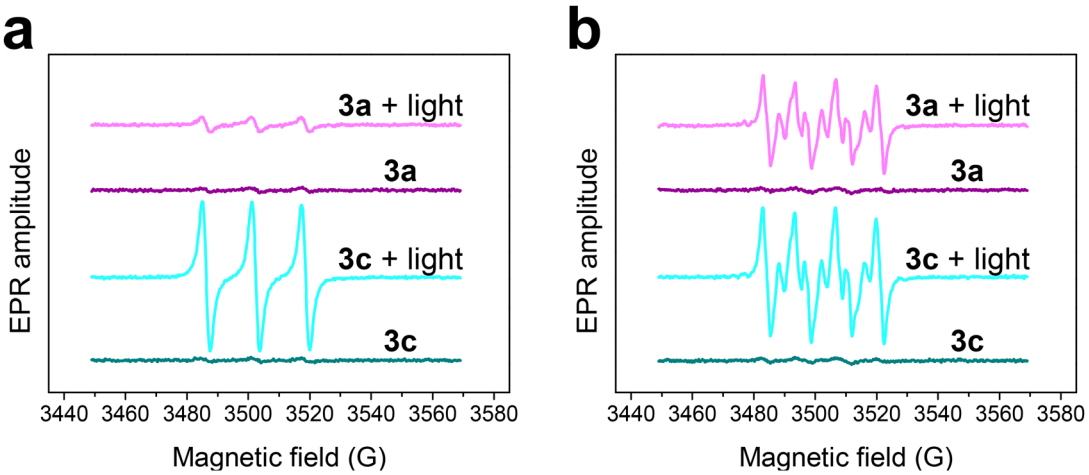

Fig. 3 EPR spectra of Ir(III)–COUPY conjugates **3a** and **3c** trapped by 4-amino-TEMP (a) or DMPO (b) in MeOH, in the dark and upon irradiation with green light (505 nm, 2 min, 100 mW cm^{-2}).

Table 1 Thermodynamic energy difference between products and reactants (ΔE) for excited-state intramolecular electron transfer and generation of superoxide anion (type I PDT) reactions. ^{1}**1a**$^+$ refers to the singlet ground state of **1a** with total molecular charge +1, ^{2}**1a**$^{2+}$ stands for the doublet ground state of **1a** with total molecular charge +2, and so on

#	Conjugate	Reaction	ΔE (eV)
		Photoinduced electron transfer	
(1)	**3a**	^{1}**1a**$^+$ (S_1) + ^{1}**2a**$^+$ → ^{2}**1a**$^{2+}$ + ^{2}**2a**^{0}	−0.100
(2)	**3b**	^{1}**1b**$^+$ (S_1) + ^{1}**2a**$^+$ → ^{2}**1b**$^{2+}$ + ^{2}**2a**^{0}	−0.298
(3)	**3c**	^{1}**1a**$^+$ (S_1) + ^{1}**2b**$^+$ → ^{2}**1a**$^{2+}$ + ^{2}**2b**^{0}	−0.102
		Superoxide formation	
(4)	**3a,3b**	^{2}**2a**^{0} + $^3O_2$ → ^{1}**2a**$^+$ + ^{2}($^\bullet O_2^-$)	−0.163
(5)	**3c**	^{2}**2b**^{0} + $^3O_2$ → ^{1}**2b**$^+$ + ^{2}($^\bullet O_2^-$)	−0.159

oxide (Fig. 3b). The fact that no paramagnetic signal was observed in the absence of light confirmed that, as in the case of $^1O_2$, the production of $O_2^{\bullet-}$ was a light-induced process.

Additional insights into the viability of the type I PDT mechanism and intramolecular photoinduced electron transfer between the coumarin moiety and the Ir(III) complex to generate a geminate radical ion pair was ascertained through density functional theory (DFT) calculations[38–42] (Tables 1, S3 and S4 and Fig. S10†). Our data show that the electron transfer processes from excited state S_1 of both COUPY coumarins (**1a**, **1b**) to the corresponding Ir(III) complexes (**2a**, **2b**) in Ir(III)–COUPY conjugates **3a–3c** are slightly thermodynamically favorable (reactions 1–3, Table 1). Even more significant is the favorable reduction of molecular dioxygen by the obtained radicals ^{2}**2a**^{0} and ^{2}**2b**^{0} forming superoxide, as confirmed by the higher electron affinity of oxygen than the Ir(III) complexes (reactions 4 and 5, Table S3†), supporting the occurrence of type I PDT activity for conjugates **3a–3c**, as experimentally observed (*vide infra*).

As expected, electron transfer mechanisms from the ground state of COUPYs toward the Ir(III) complex can definitely be ruled out on the basis of our computed thermodynamic data (see Table S4†), confirming the necessity to reach the excited state localized over the coumarin fragment to promote such a mechanism.

The optimized structure of **3c** in water reveals specific non-covalent interactions that reduce the molecular volume of the conjugate (Fig. 4). These include the C–H···O=C H-bonding-like interaction, C–H···π (T-shape)[43] interactions involving the C–H bonds of the tertiary amine ethyl groups, and C–F···H–C electrostatic interactions. Overall, this molecular packing should favour small distances between the COUPY moiety and the Ir(III) metal centre, facilitating photoinduced electron transfer processes between both components of the Ir(III)–COUPY conjugate.

Dark and light stability of Ir(III)–COUPY conjugates in biological media

The stability of the Ir(III)–COUPY conjugates **3a–c** in DMEM culture medium supplemented with 10% FBS was evaluated by reversed-phase HPLC in the dark and upon red light irradiation. The three compounds were remarkably stable in the dark even for 48 h at 37 °C (Fig. S11–S15†). Furthermore,

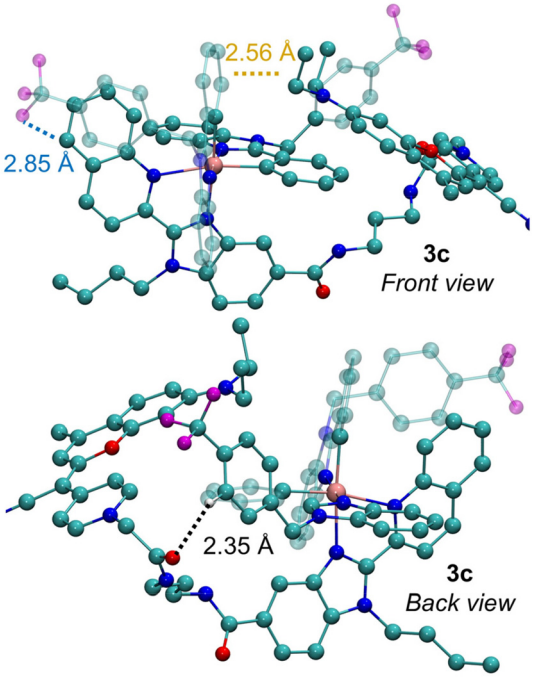

Fig. 4 3D structure of **3c** in water. H-bonding-like C–H···O=C, C–H···π, and C–F···H–C interactions are highlighted in black, orange, and blue, respectively. Hydrogen atoms are omitted for the sake of clarity.

while compound **3b** displayed considerable photodegradation after 1 h under irradiation with red light (620 ± 15 nm; 130 mW cm^{-2}), less than 20% photobleaching was observed for compounds **3a** and **3c** (Fig. S11 and S16–S18†), which indicated that the incorporation of the julolidine moiety into the coumarin backbone had a negative effect on the overall photostability of the compounds.

Cellular uptake and subcellular localization

The cellular accumulation of the Ir(III)–COUPY conjugates **3a–3c** in cancer cells was first studied by inductively coupled plasma mass spectrometry (ICP-MS). As shown in Fig. S19,† intracellular amounts of metal content determined by ICP-MS following 2 h incubation with **3c** was approximately 6-fold higher than those found in cisplatin-treated cancer cells but comparable to other Ir(III)–COUPY conjugates *i.e.*, **3a** and **3b**, and similar to the Ir(III) parent complexes,[29] indicating good membrane permeability and cellular accumulation despite their relatively high molecular weight. Confocal microscopy was then used to gain more insights into cellular uptake and subcellular localization of the compounds in living cancer cells by taking advantage of the luminescence properties of the coumarin moiety, allowing the use of yellow light laser (λ_{ex} = 561 nm) excitation. As shown in Fig. 5, the Ir(III)–COUPY conjugate **3c** efficiently stained HeLa cells after 30 min of incubation, predominantly accumulating in the plasma membrane and, to a lesser extent, in intracellular vesicles. This behavior is consistent with the previously observed staining patterns of other Ir(III)–COUPY conjugates, including **3a** and **3b**.

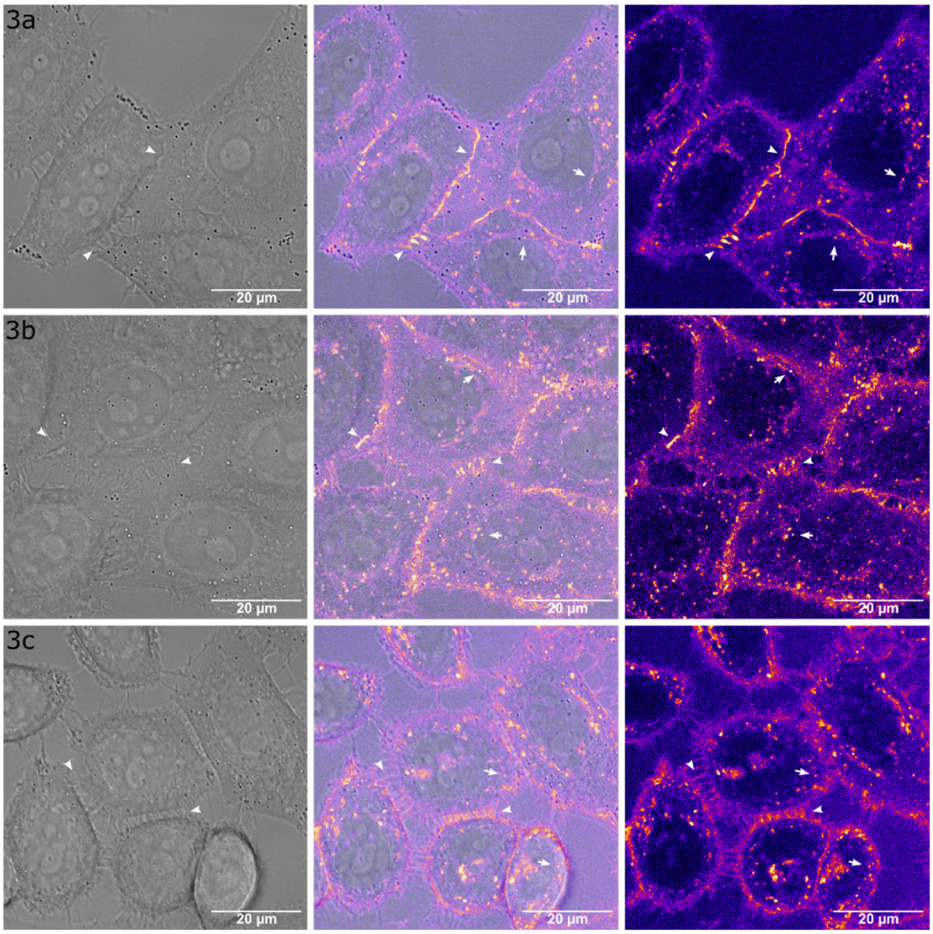

Fig. 5 Cellular uptake of Ir(III)–COUPY conjugates **3a–3c** in HeLa cells. Single confocal planes show cells treated with the compounds (5 μM) for 30 min at 37 °C. For each compound: confocal plane showing the brightfield image (left), the merged brightfield and fluorescence image (center) and the fluorescence image alone (right). The fluorescent signal (λ_{Ex} = 561 nm, λ_{Em} = 570–660 nm) is displayed using the Fire LUT. Arrows indicate cellular vesicles, and arrowheads highlight the extracellular membrane. Scale bar: 20 μm.

To better understand the nature of the intracellular vesicles stained by conjugates **3a–c**, a series of colocalization experiments were conducted using the lysosome-specific fluorescent marker LysoTracker Green DND (LTG), and the fluorescent probe wheat germ agglutinin Alexa Fluor 633 (WGA), which had affinity for glycoproteins and stained the extracellular membrane and endosomes as they formed by endocytosis. Colocalization was measured using Pearson's correlation coefficient (Table S5†).[44] As shown in Fig. 6, the three Ir(III)–COUPY conjugates exhibited a significant correlation with WGA staining (**3a**: PCC = 0.70; **3b**: PCC = 0.51; **3c**: PCC = 0.69; Table S5†). We then performed a more detailed colocalization analysis at the vesicle level and observed a lower correlation between the vesicular component of the fluorescent signals of compounds **3a–3c** and that of WGA (**3a**: PCC = 0.42; **3b**: PCC = 0.44; **3c**: PCC = 0.36; Table S5†), however, this correlation was clearly higher than that with LTG (**3a**: PCC = 0.07; **3b**: PCC = 0.03; **3c**: PCC = 0.12; Table S5†). These results suggest that the intracellular vesicles stained by compounds **3a–3c** correspond to endosomes, rather than lysosomes.

Photobiological studies

To evaluate the photocytotoxicity of the compounds, cisplatin-resistant ovarian cancer (A2780cis) cells were first chosen. The resistance of A2780cis cells is caused by elevated levels of the antioxidant glutathione tripeptide and altered DNA repair mechanism.[45,46] This provides an interesting biological system to model the efficacy of Ir(III)–COUPY PSs in a challenging intracellular reductant environment that scavenges excess reactive oxygen species (ROS) and fails to activate apoptosis in response to oxidative damage caused by ROS. As shown in Table 2 and Fig. S21,† all compounds including the parent Ir(III) complexes (**2a**, **2b**), COUPY coumarin **1a** and Ir(III)–COUPY conjugates (**3a–3c**) were deemed to be inactive (>250 μM) against A2780cis cells under dark conditions, with the exception of COUPY **1b**, which bore the julolidine-fused system. Next, we determined the half-maximal inhibitory concentration (IC_{50}) values of the compounds upon 1 h irradiation with red light centered at 620 nm and compared them with our previously reported results using green light (520 nm).[29]

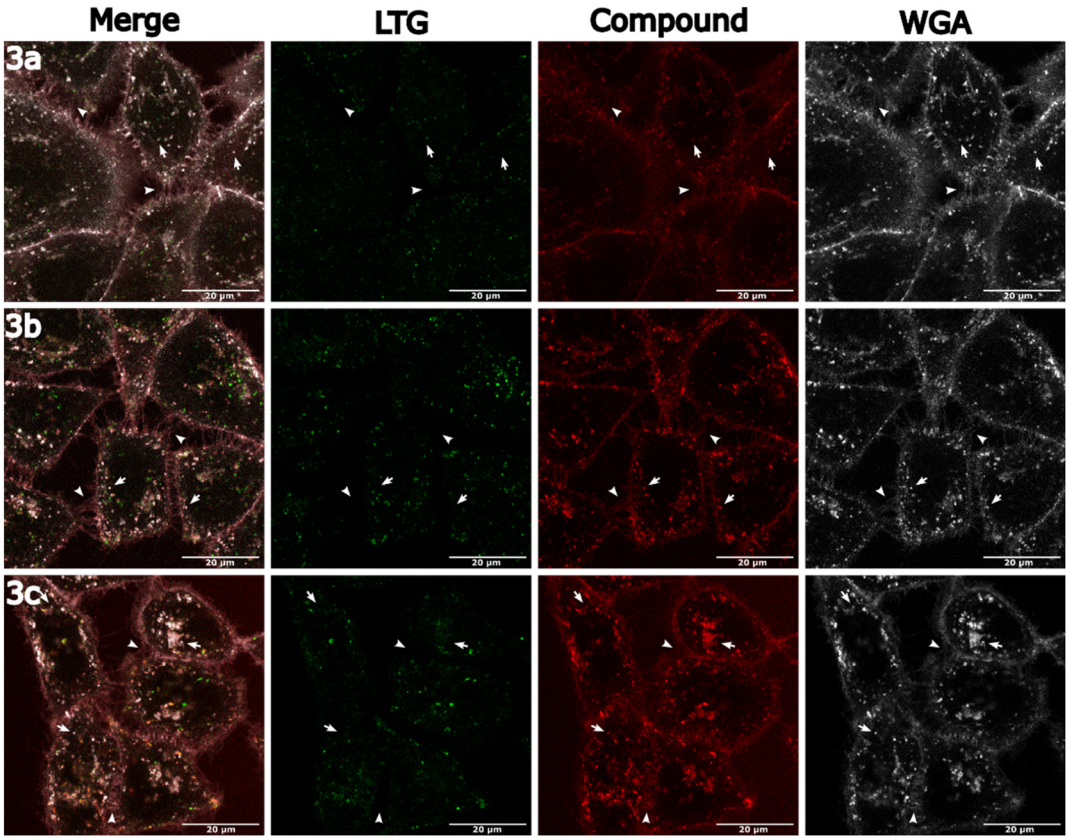

Fig. 6 Colocalization studies of Ir(III)–COUPY conjugates **3a–3c** with LTG and WGA. Single confocal planes show HeLa cells incubated with the corresponding conjugate (5 µM, 30 min at 37 °C, λ_{Ex} = 561 nm, λ_{Em} = 570–660 nm, red), LTG (0.5 µM, 5 min at 37 °C, λ_{Ex} = 488 nm, λ_{Em} = 500–550 nm, green) and WGA (2 µg mL^{-1}, 20 min at 37 °C, λ_{Ex} = 633 nm, λ_{Em} = 660–760 nm, grey). Left: merged images; center left: LTG signal; center right: compound signal; right: WGA signal. Arrows indicate colocalizing compound–WGA vesicles, and arrowheads highlight the extracellular membrane. Scale bar: 20 µm.

Table 2 Photocytotoxicity of the compounds under study towards A2780cis cancer cells[a]

	IC_{50} (µM), dark	IC_{50} (µM), 520 nm	PI[b]	IC_{50} (µM), 620 nm	PI[b]
1a	>250	2.1 ± 0.2[c]	>119	7.1 ± 0.4	>35
1b	15 ± 2	0.15 ± 0.04[c]	100.0	0.7 ± 0.1	21.4
2a	>250	1.5 ± 0.1	>166.7	4.5 ± 0.3	>56
2b	>250	3.5 ± 0.4[c]	>71	9 ± 2	>28
3a	>250	0.7 ± 0.06[c]	>357	0.71 ± 0.02	>352
3b	>250	1.04 ± 0.02[c]	>240	1.2 ± 0.1	>208
3c	>250	1.9 ± 0.3	>134	1.2 ± 0.2	>208

[a] Cells were treated for 2 h (1 h incubation and 1 h irradiation with green or red light at 520 nm or 620 nm, respectively) followed by 48 h of incubation in drug-free medium. Dark analogues were kept in the dark. Data expressed as mean ± SD from three independent experiments. [b] PI = phototherapeutic index defined as IC_{50} (dark-non-irradiated cells)/IC_{50} (irradiated cells). [c] Data reported in ref. 29.

The phototherapeutic index (PI), calculated as the ratio of dark to light IC_{50} values, was considered as the measure for light-induced cytotoxicity. Interestingly, the photocytotoxicities of the Ir(III)–COUPY conjugates upon 620 nm light irradiation were very similar to those obtained with 520 nm light (IC_{50} values between 0.7 and 1.2 µM compared to 0.7–1.9 µM, respectively) using similar light doses (5.4 and 6.7 J cm^{-2} with 520 nm and 620 nm light, respectively). In contrast, a 3- to 5-fold loss in photocytotoxicity was found for the parent compounds (Ir(III) complexes and COUPY dyes) when changing from 520 nm light to 620 nm light irradiation (Table 2). As a result, similar PI values were obtained for **3a** and **3b** following red light treatment (>352 and >208, respectively) compared to green light treatment (>357 and >240, respectively, Table 2 and Fig S21†). Strikingly, the photocytotoxicity of **3c** under red light provided a higher PI than that under green light (>208 *vs.* >134). This *in vitro* anticancer photoactivity retention upon irradiation with longer wavelengths of light indicated the potential of Ir(III)–COUPY conjugates for red-light PDT.

In view of this, we decided to explore the ability of the Ir(III)–coumarin PSs to overcome the hypoxia limitation. The A2780cis cells were incubated under hypoxic conditions (2% O_2) and dosed with compounds **3a–3c** under dark and light treatment regimens (Table S6†). As depicted in Fig. 7, all three conjugates exhibited potent photocytotoxicity under hypoxia, with IC_{50} values in the low micromolar range.

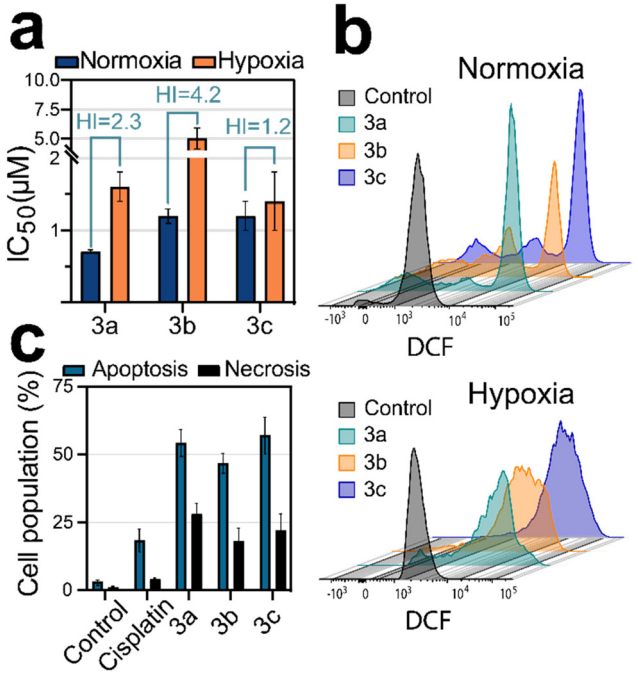

Fig. 7 Photobiological evaluation of Ir(III)–COUPY PSs **3a–3c**. (a) *In vitro* photocytotoxicity under normoxia (21% O_2) or hypoxia (2% O_2) conditions, as measured by half-maximal inhibitory concentrations (IC_{50}) in A2780cis cells after red light irradiation. Data shown as mean ± SD from three independent experiments. (b) Representative histograms of DCFH-DA-stained A2780cis cells after PDT treatments with **3a–3c** (10 μM, 1 h) on the FL1-H channel (λ_{exc} = 488 nm and λ_{em} = 530 ± 30 nm). (c) Cell death induction in A2780cis after PDT treatment with **3a–3c**. Data from three independent flow cytometry experiments using annexin V/PI dual staining. AV^+/PI^- and AV^+/PI^+ were considered as apoptotic cells, and AV^-/PI^+ as necrosis. Light irradiation conditions: 620 nm light, 15 mW cm^{-2}, 1 h.

Notably, 5-aminolevulinic acid (5-ALA), the clinically approved precursor of the protoporphyrin IX (PpIX) PS, was barely active under normoxic conditions and inactive under hypoxic conditions. To better illustrate the oxygen sensitivity of the studied PSs, we used the hypoxia index (HI), *i.e.*, the ratio of the light IC_{50} value under normoxia to that under hypoxia.[29] Strikingly, the HI for **3a** was 2.3, indicating that hypoxic conditions halved its photocytotoxicity, whereas the HI for **3b** was ~4, meaning a 4-fold loss in photoactivity under low oxygen concentration (Fig. 6a). In contrast, **3c** displayed a HI close to 1, which indicated that the photocytotoxicity of **3c** was not entirely dependent on high oxygen concentrations.

Based on the promising results obtained in A2780cis cells, we focused on evaluating the biological photoactivity of Ir(III)–COUPY conjugates **3a–3c** in the mammary cancer cell line EO771 with the aim of further validating their efficacy for red-light under hypoxic conditions. To our delight, the conjugates showed a similar trend in photocytotoxicity (Table 3). Notably, **3c** exhibited the largest PI values (>227) under hypoxia and the smallest HI (1.1), which led us to select **3c** as the best PS.

Table 3 Photocytotoxicity towards EO771 cells under normoxia and hypoxia conditions[a]

	Normoxia (21% O_2)			Hypoxia (2% O_2)			
	IC_{50} (μM), Dark	IC_{50} (μM), 620 nm	PI[b]	IC_{50} (μM), Dark	IC_{50} (μM), 620 nm	PI[b]	HI[c]
3a	>250	1.7 ± 0.3	>147	>250	3.1 ± 0.9	>81	1.8
3b	>250	2.3 ± 0.1	>109	>250	3.8 ± 0.6	>66	1.7
3c	>250	0.98 ± 0.17	>255	>250	1.1 ± 0.1	>227	1.1

[a] Cells were treated for 2 h (1 h incubation and 1 h irradiation with red light) followed by 48 h of incubation in drug-free medium either under normoxic (21% O_2) or hypoxic (2% O_2) conditions. Dark analogues were kept in the dark. Data expressed as mean ± SD from three independent experiments. [b] PI = phototherapeutic index defined as IC_{50} (dark-non-irradiated cells)/IC_{50} (irradiated cells). [c] HI = hypoxia index defined as the ratio of IC_{50} values obtained under hypoxic (2% O_2) and normoxic (21% O_2) conditions after light irradiation.

To gain insights into the ability of **3c** to overcome the barrier of hypoxia, the levels of intracellular ROS were measured after red light irradiation under normoxic and hypoxic conditions in A2780cis and EO771 cells and were then compared to those raised by the two previously reported conjugates (**3a**, **3b**). Interestingly, all Ir(III)–COUPY conjugates rapidly photogenerated a large amount of ROS under both conditions, as revealed by strong intracellular fluorescent signals of the DCFH-DA probe compared to non-treated cells (Fig. 7b and Fig. S22 and S23†). As such, if $^1O_2$ generation was the primary mediator of photocytotoxicity, then hypoxia would diminish ROS levels because the lack of oxygen would dramatically limit type II PDT reactions. However, although ROS photogeneration was considerably lower under hypoxic conditions, significant differences between the control and treated groups were still found (Fig. 7b). Such differences, ranging from 2- to 3-fold increases in overall ROS levels, were somewhat comparable to those found under normoxic conditions, which showed approximately 3-fold changes in both A2780cis and EO771 cell lines (Fig. S22 and S23†). This situation would be compatible with type I and type II PDT mechanisms simultaneously operating under low oxygen environments. To further verify this hypothesis, selective scavengers of reactive species were used, *i.e.*, sodium azide (NaN_3) for $^1O_2$, MnTBAP for $O_2^{\bullet-}$ and terephthalic acid for $^{\bullet}OH$, upon PDT treatment with **3a–3c** (Fig. S23 and S24†). We found that MnTBAP and terephthalic acid partially inhibited fluorescence enhancement of DCF regardless of the low oxygen concentration, which suggested that type I superoxide and hydroxyl radical species participated in the reaction mechanism. As expected, NaN_3 treatment only prevented ROS photogeneration with **3a–3c** under normoxic conditions but not under hypoxic conditions, which could imply a minor role of $^1O_2$ under hypoxia and an overall shift toward type I PDT.

Photoredox catalysis in cells could also be the main underlying mechanism of PDT, especially in oxygen-depleted environments.[47] Nicotinamide adenine dinucleotide (NADH),

a key reducing metabolite that participates in the mitochondrial electron transport chain, is considered to be the main biological electron donor in photosensitization.[35,47] As a result, photocatalytic conversion of NADH in cancer cells has been proposed as a promising anticancer strategy.[35,48–50] In this context, we evaluated the photocatalytic oxidation of NADH by Ir(III)–COUPY conjugates **3a–3c** in PBS by UV-Vis spectroscopy, according to previously described methods.[50] As shown in Fig. S26,† the spectrum of NADH (160 μM) remained unchanged after 5 min of incubation with conjugates **3a–3c** (10 μM) in the dark at 37 °C. Conversely, upon irradiation with red light (620 ± 15 nm; 130 mW cm^{-2}), compounds **3a–c** dramatically reduced the absorption of NADH (Fig. S26†). The turnover frequency (TOF) values of **3a–3c** after 5 min of light irradiation were 179, 164 and 152 h^{-1} (Fig. S27†), respectively, which were in the same range as those for other Ir(III) complexes described in the literature.[49,50] Therefore, the high photocytotoxicity of Ir(III)–COUPY conjugates could be attributed not only to the photogeneration of ROS but also to the photocatalytic oxidation of NADH.

The high photocytotoxicity of Ir(III)–COUPY conjugates was already revealed in confocal microscopy studies by monitoring the morphological changes to the cells after laser irradiation. As shown in Fig. S20,† plasma membrane rupture and blebbing were observed in all cases. Additionally, flow cytometry analysis revealed secondary populations of A2780cis with reduced cell size as detected in forward light scattering (FSC) and nuclear and cytoplasmic condensation as shown by the transient increase in side scattering (SCC), indicating an overall disruption of normal cell morphology accompanied by cell shrinkage after red-light treatments (Fig. S28 and S29†). To discern the type of cell death induced, dual annexin V/propidium iodide (AV/PI) staining was employed (Fig. 7c and Fig. S30†), showing large A2780cis populations undergoing phosphatidylserine translocation after PDT treatments (AV^+/PI^- and AV^+/PI^+ populations). Altogether, these morphological signatures indicated beyond doubt that apoptosis was the main cell death mode of action induced by red-light PDT with these PSs. This was somewhat intriguing because our previous results using the same irradiation protocol but with 520 nm light (1.5 mW cm^{-2}) showed necrosis photoinduction.[29] We note that the cell death mode of PSs depends on the PDT dose applied, *i.e.*, PS concentration and light fluence, but the fact that opposite types of cell death (necrosis *vs.* apoptosis) can be induced depending on the wavelength and intensity of light applied using structurally similar PSs is interesting for several reasons. On the one hand, the ability to cause effective cancer cell death upon irradiation at different wavelengths of light demonstrates that Ir(III)–COUPYs behave as polychromatic compounds, which might enable optimization of the light parameters and protocols according to treatment depth requirements. On the other hand, activation of apoptosis upon red-light irradiation in A2780cis cells, which intrinsically show resistance to cisplatin-induced apoptosis (Fig. 7c), is promising for resistant cancers where chemotherapy alone might be inefficient.

Phototherapeutic efficacy in 3D tumor spheroids and *in vivo* toxicity

Encouraged by these promising results with the best performing Ir(III)–COUPY conjugate, **3c**, we decided to evaluate its phototherapeutic efficacy in a 3D tumor spheroid model, as well as that of **3a** and **3b** for comparison purposes. Tumor spheroids mimic hypoxia features of growing tumors under pathophysiological conditions owing to oxygen gradients towards the center of the sphere.[51] The efficacy of the PSs in EO771 multicellular tumor spheroids (MCTS) was evaluated by monitoring growth in volume as well as spheroid viability after PDT over a span of 8 days. After red-light irradiation, the growth of these MCTS treated with **3a** and **3c**, and to a lesser extent with **3b** was impaired (Fig. 8 and S31†). To confirm cell death induction in spheroids with Ir(III)–COUPY PDT, calcein-AM/propidium iodide dual staining was performed. As illustrated in Fig. S32,† a reduction in calcein-AM fluorescence with a concomitant increase in propidium iodide fluorescence was observed in PDT-treated MCTS, particularly with **3c**, revealing a high proportion of dead cells with compromised membrane integrity.

Given the phototherapeutic performance of **3c**-PDT, we conducted a preliminary *in vivo* toxicological study to assess its biocompatibility. In this study, conjugate **3c** was administered intraperitoneally at a dose of 5 mg kg^{-1} to both male and female C57BL6/Hsd mice. The mice were monitored for 7 days for mortality, morbidity, body weight changes, and other signs of treatment-related toxicity. To our delight, Ir(III)–COUPY conjugate **3c** was well tolerated by both sexes throughout the study. As shown in Fig. 9, there were no significant differences in body weight between the control (Vh) and **3c**-treated groups. Post-mortem examination of organs revealed no significant abnormalities. Additionally, biochemistry analysis of the plasma samples showed no significant differences between the control and treated groups (Fig. S33†). Overall, there were no signs of toxicity or adverse effects, indicating that the 5 mg kg^{-1} dose was well tolerated. These preliminary studies will serve as the basis for the design of an *in vivo* phototherapeutic efficacy study with Ir(III)–COUPY conjugates using red light.

Experimental section

Synthesis of Ir(III)–COUPY conjugate 3c

Ir(III) complex 4 (Ir–COOH). The cyclometalated iridium(III) chloro-bridged dimer[13] (93 mg, 50 μmol) and the N^N ligand methyl 1-butyl-2-(quinolin-2-yl)-1*H*-benzo[*d*]imidazole-5-carboxylate[27] (36 mg, 105 μmol) were dissolved in DCM/MeOH (2 : 3, v/v) in a Schlenk flask. The reaction was stirred at 58 °C for 24 h under a nitrogen atmosphere. After cooling the solution to room temperature, an excess of KPF_6 (125 μmol) was added and it was stirred for 30 min. The solvent was concentrated under reduced pressure, and the product was washed with water and recrystallized using DCM and diethyl ether to give 58 mg of a red solid (yield: 84%). ^1H NMR (400 MHz, DMSO-d_6): δ 8.91 (d, J = 8.6 Hz, 1H), 8.68 (d, J = 8.6 Hz, 1H),

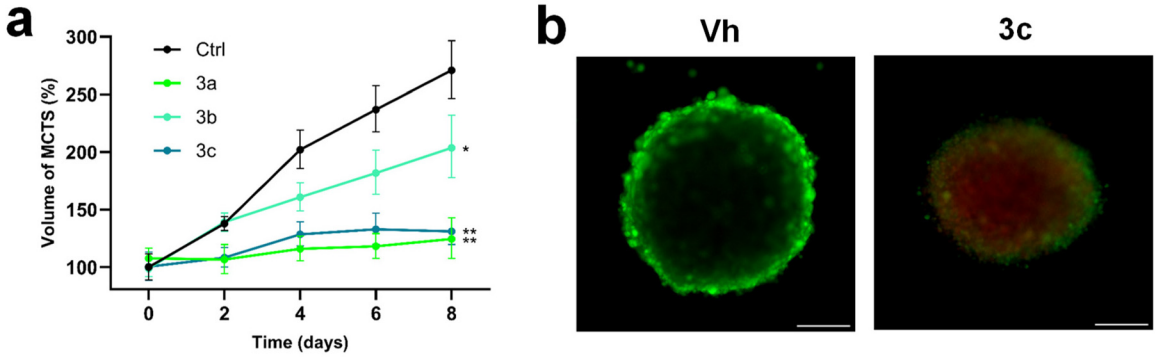

Fig. 8 Ir(III)–COUPY PDT on mammary tumor spheroids. (a) Change in the relative volume of EO771 multicellular tumor spheroids treated with conjugates **3a**, **3b**, and **3c** at a concentration of 20 μM every second day over a period of 8 days under red-light irradiation. Error bars indicate SD from three replicates. Statistical significance (*$p < 0.05$, **$p < 0.01$, ***$p < 0.001$) was determined using a one-way ANOVA test. (b) Representative image of EO771 spheroids treated with vehicle (Vh) or 20 μM concentrations of **3c** for 1 h. Calcein AM (green) was used for live cell staining and propidium iodide (red) for dead cell staining. Scale bar = 200 μm. Light irradiation conditions: 620 nm light, 15 mW cm^{-2}, 1 h.

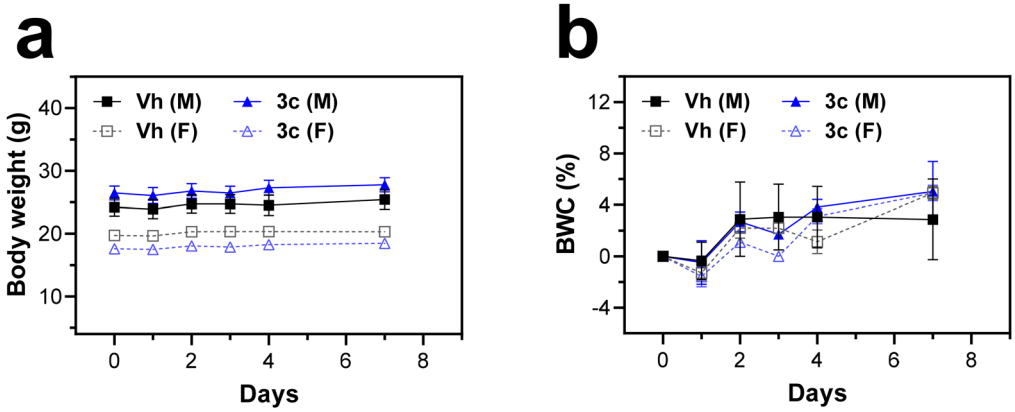

Fig. 9 Toxicological *in vivo* study of conjugate **3c** in C57BL6/Hsd mice. The evolution of (a) body weight and (b) body weight change (BWC) were monitored in both male (M) and female (F) mice ($n = 3$ per group) following an acute intraperitoneal injection of compound **3c** (5 mg kg^{-1}) compared to a vehicle (Vh) control. Mice were sacrificed 7 days post-treatment. Values are presented as mean ± SEM.

8.20 (d, $J = 8.0$ Hz, 1H), 8.10–8.01 (m, 3H), 7.84 (d, $J = 7.6$ Hz, 1H), 7.76 (d, $J = 7.6$ Hz, 1H), 7.72–7.68 (m, 2H), 7.65 (t, $J = 7.6$ Hz, 1H), 7.56 (d, $J = 8.4$ Hz, 2H), 7.46 (d, $J = 8.4$ Hz, 2H), 7.21 (t, $J = 8.3$ Hz, 2H), 7.13–7.10 (m, 3H), 7.02 (d, $J = 8.3$ Hz, 3H), 6.98–6.92 (m, 2H), 6.90–6.83 (m, 4H), 6.44 (d, $J = 6.7$ Hz, 1H), 6.35–6.30 (m, 2H), 6.25–6.13 (m, 4H), 6.05 (d, $J = 8.4$ Hz, 1H), 5.16–4.95 (m, 2H), 1.75–1.54 (m, 2H), 0.94–0.72 (m, 2H), 0.54 (t, $J = 7.2$ Hz, 3H). ^{13}C NMR (150 MHz, DMSO-d_6): δ 166.4, 162.8, 162.1, 156.0, 154.2, 149.8, 148.1, 145.0, 141.6, 140.9, 140.7, 139.1, 139.0, 138.4, 138.3, 134.9, 134.8, 133.3, 132.5, 131.4, 130.5, 130.3, 129.3, 129.0, 128.4, 128.1, 126.6, 126.5, 126.0, 125.8, 125.5, 125.4, 125.3, 124.4, 123.9, 123.1, 122.7, 122.6, 122.0, 120.8, 120.1, 113.8, 113.7, 112.9, 111.9, 111.8, 46.7, 46.7, 45.9, 31.7, 18.8, 13.3. HRMS (ESI-TOF) m/z: $[M - PF_6]^+$ calcd for $C_{63}H_{47}F_{12}IrN_7O_2P$ 1240.332; found 1240.3284.

Ir(III)–COUPY conjugate 3c. To a solution of Ir(III) complex **4** (11 mg, 7.98 μmol) and HATU (3.1 mg, 7.98 μmol) in anhydrous DMF (2 mL) under an Ar atmosphere, DIPEA (3 μL, 16.1 μmol) was added and the mixture was stirred for 10 min under Ar at room temperature and protected from light. After addition of a solution of coumarin **5** [27] (12,4 mg, 23.9 μmol) and DIPEA (7 μL, 40.3 μmol) in anhydrous DMF (3 mL), the reaction mixture was stirred for 2.5 h at room temperature under Ar and protected from light. After evaporation under reduced pressure, the crude product was purified by column chromatography (silica gel, 0–12% MeOH in DCM) to give 10.7 mg of a purple solid (yield: 73%). TLC: R_f (10% MeOH in DCM) 0.54. ^{1}H NMR (400 MHz, DMSO-d_6) δ (ppm) 9.03 (1H, br. s), 8.92 (1H, d, $J = 8.8$ Hz), 8.76 (1H, t, $J = 5.4$ Hz), 8.69 (1H, d, $J = 8.9$ Hz), 8.56 (2H, d, $J = 7.4$ Hz), 8.18 (4H, m), 8.04 (1H, d, $J = 9.1$ Hz), 7.94 (2H, t, $J = 8.9$ Hz), 7.81 (1H, d, $J = 8.4$ Hz), 7.72 (4H, m), 7.62 (1H, t, $J = 7.9$ Hz), 7.54 (4H, d, $J = 8.4$ Hz), 7.21 (4H, m), 7.03 (4H, m), 6.88 (8H, m), 6.61 (1H, s), 6.23 (7H, m), 5.90 (1H, d, $J = 8.3$ Hz), 5.30 (2H, s), 5.09 (2H, m), 3.53 (4H, m), 3.15 (4H, m), 2.55 (3H, s), 1.67 (4H, m), 1.15 (5H, m), 0.85 (2H, m), 0.56 (3H, t, $J = 7.2$ Hz). ^{13}C NMR (101 MHz, DMSO-d_6) δ (ppm) 166.8, 165.6, 165.0, 162.8, 162.2, 155.6, 154.9, 154.3, 152.8, 152.0, 149.8, 149.2, 148.0, 145.5, 144.2, 141.5, 140.8,

139.1, 138.6, 138.1, 138.0, 135.0, 134.8, 133.5, 133.4, 132.9, 132.2, 132.1, 131.2, 130.5, 130.3, 129.2, 129.0, 128.4, 128.1, 128.0, 127.0, 127.0, 126.3, 125.9, 125.7, 125.7, 125.7, 125.6, 125.3, 124.8, 124.3, 123.9, 123.7, 122.7, 122.6, 122.0, 120.7, 120.1, 118.2, 117.5, 114.1, 113.4, 112.8, 111.9, 111.8, 110.4, 110.4, 96.5, 78.1, 59.6, 53.4, 46.2, 44.2, 41.6, 37.1, 37.0, 31.8, 29.0, 28.9, 18.9, 18.7, 18.4, 18.0, 16.7, 13.3, 12.4, 12.3. HRMS (ESI-TOF) m/z: $[M]^{2+}$ calcd for $C_{89}H_{77}F_6IrN_{12}O_3$ 834.2885, found 834.2887. Analytical HPLC (10 to 100% B in 6 min, formic acid additive): t_R = 2.85 min.

Photophysical and photochemical characterization of the compounds

Spectroscopic characterization. For photophysical measurements, all solvents used were of spectroscopic grade. Absorption spectra were recorded on a Varian Cary 500 UV/Vis/NIR or Varian Cary 6000i spectrophotometer at room temperature. Molar absorption coefficients (ε) were determined by direct application of the Beer–Lambert law, using solutions of the compounds in each solvent with concentrations ranging from 10^{-6} to 10^{-5} M. Emission spectra were recorded on a Photon Technology International (PTI) fluorimeter or in a Horiba Fluoromax-4 spectrofluorometer. Fluorescence quantum yields (Φ_F) were measured by a comparative method using cresyl violet in ethanol (CV; $\Phi_{F;Ref}$ = 0.54 ± 0.03) as the reference.[52–54] Then, optically matched solutions of the compounds and CV were excited and the fluorescence spectra were recorded. The absorbance of sample and reference solutions was set below 0.1 at the excitation wavelength and Φ_F was calculated using the following eqn (1):

$$\Phi_{F;Sample} = \frac{Area_{Sample}}{Area_{Ref}} \times \left(\frac{\eta_{Sample}}{\eta_{Ref}}\right)^2 \times \Phi_{F;Ref} \quad (1)$$

where $Area_{Sample}$ and $Area_{Ref}$ are the integrated fluorescence for the sample and the reference and η_{Sample} and η_{Ref} are the refractive indexes of sample and reference solutions respectively. The uncertainty in the experimental value of Φ_F was estimated to be approximately 10%.

Phosphorescence quantum yields (Φ_P) of the iridium complex were determined analogously to Φ_F, using argon-saturated *meso*-tetra-5,10,15,20-phenylporphine as the reference (Φ_F = 0.11 in toluene).[55]

Singlet oxygen quantum yield determination. Singlet oxygen generation was studied by time-resolved near-infrared phosphorescence by means of a customised setup. Briefly, a pulsed Nd:YAG laser (FTSS355-Q, Crystal Laser, Berlin, Germany) working at a repetition rate of 1 or 10 kHz at 355 nm (0.5 μJ per pulse) or 532 nm (1.2 μJ per pulse) was used to excite the sample. A 1064 nm rugate notch filter (Edmund Optics) and an uncoated SKG-5 filter (CVI Laser Corporation) were placed in the laser path to remove any NIR emission. The light emitted by the sample was filtered with a 1000 nm long-pass filter (Edmund Optics) and later by a narrow bandpass filter at 1275 nm (BK-1270-70-B, bk Interferenzoptik). A thermoelectric-cooled NIR-sensitive photomultiplier tube assembly (H9170-45, Hamamatsu Photonics, Hamamatsu, Japan) was used as the detector. Photon counting was achieved with a multichannel scaler (NanoHarp 250, PicoQuant). The time dependence of the $^1O_2$ phosphorescence with the signal intensity, $S(t)$, is described by eqn (2), in which τ_T and τ_Δ are the lifetimes of the photosensitizer triplet state and of $^1O_2$ respectively, and S_0 is a preexponential parameter proportional to Φ_Δ.

$$S_{1275}(t) = S_{1275}(0) \times \frac{\tau_\Delta}{\tau_\Delta - \tau_T} \times \left(e^{-t/\tau_\Delta} - e^{-t/\tau_T}\right) \quad (2)$$

The Φ_Δ values of different samples were obtained by comparing S_0 values of optically matched samples and using an appropriate reference, by means of eqn (3).

$$\Phi_{\Delta,Sample} = \Phi_{\Delta,Ref} \times \frac{S_{0,Sample}}{S_{0,Ref}} \quad (3)$$

The same setup was used to monitor the phosphorescence of the complex and the conjugate, except that the red-sensitive Hamamatsu H5783 photosensor module was used for detection.

Superoxide anion radical generation and characterization. DHR123 (10 μM) was added to solutions of Ir(III)–COUPY conjugates **3a–3c** (10 μM) in PBS containing 2% DMSO. The fluorescence spectra of the resulting solutions upon excitation at 500 nm were recorded from 510 to 600 nm (DHR123: λ_{Ex} = 507 nm, λ_{Em} = 529 nm) before (dark) and after irradiation with red light (620 ± 15 nm; 130 mW cm^{-2}) for the indicated time intervals (1, 2, 3, 4 and 5 min). Negative control experiments were carried out using PBS alone and solutions of Ir(III)–COUPY conjugates **3a–3c** in PBS saturated with sodium 4,5-dihydroxybenzene-1,3-disulfonate (tiron), a superoxide anion radical scavenger. Fluorescence emission spectra of the various samples were recorded on a Photon Technology International (PTI) QuantaMaster fluorometer at room temperature. The entrance and exit slits of the excitation and emission monochromators were set at 0.5 mm, giving a spectral bandwidth of 2 nm. The data interval was 1 nm and the integration time was 1 s. All measurements were carried out using a Hellma 1.5 mL PTFE-stoppered fluorescence quartz cuvette (4 clear windows) with a 1 cm path length.

Electron paramagnetic resonance studies. Briefly, the corresponding Ir(III)–COUPY conjugate (250 μM) was dissolved in MeOH containing either 60 mM 4-amino-TEMP (4-amino-2,2,6,6-tetramethylpiperidine) as a spin trap for $O_2^{\bullet-}$, or 360 mM DMPO (5,5-dimethyl-1-pyrroline-*N*-oxide) as a spin trap for $^1O_2$, and the resulting samples were loaded into Q-band Suprasil® quartz EPR capillary tubes with 1 mm internal diameter, with both ends open, and sealed with Critoseal®. EPR spectra were recorded in the dark and after 2 min of irradiation with a high-power green LED (505 nm, 100 mW cm^{-2}). EPR spectra were recorded on a Bruker Elexys 580 spectrometer working at the X-band at room temperature. All spectra were collected under a continuous-wave (CW) regime using a Bruker ER4122 SHQE superhigh-Q cylindrical resonator. The microwave frequency was 9.858 GHz, and both the modulation amplitude (0.1 mT) and the microwave power

(4.7 mW) were selected in such a way that no distortion or saturation of the signal was produced.

Photooxidation of NADH. Ir(III)–COUPY conjugates **3a–3c** (10 μM) were added to solutions of NADH (160 μM) in PBS containing 2% DMSO. The absorption spectra of the resulting solutions were recorded from 240 to 490 nm before (dark) and after irradiation with red light (620 ± 15 nm; 130 mW cm^{-2}) for the indicated time intervals (1, 2, 3, 4 and 5 min). Absorption spectra of the various samples were recorded on a Jasco V-730 UV-Vis spectrophotometer at room temperature. The spectral bandwidth was 1 nm, the data interval was 0.2 nm, the response time was 0.24 s and the scan speed was 200 nm min^{-1}. All measurements were carried out using a Hellma 1.5 mL PTFE-stoppered fluorescence quartz cuvette (4 clear windows) with a 1 cm path length.

The turnover number (TON) and the turnover frequency (TOF) values were calculated following eqn (4) and (5), respectively. The concentration of NADH was obtained following Lambert–Beer's law. The extinction coefficient of NADH in water at 339 nm is 6220 M^{-1} cm^{-1}.[56]

$$\mathrm{TON} = \left(\frac{\text{no. mols of NADH converted}}{\text{no. mols of Ir(III) complex used}}\right) \quad (4)$$

$$\mathrm{TOF} = \left(\frac{\mathrm{TON}}{\text{time (h)}}\right) \quad (5)$$

Computational studies. Geometry optimizations of **1a**, **1b**, **2a**, and **2b** were conducted at the density functional theory (DFT) level by means of the PBE0[38] functional with D3 dispersion[39] corrections as implemented in Gaussian 16[40] and without symmetry restrains. The employed basis set for systems **1a** and **1b** was 6-31G*, whereas systems **2a** and **2b** were described with the 6-31+G(d,p) basis set for all atoms except Ir, which was treated with the Stuttgart–Dresden pseudopotential[41] (hereafter, PBE0/6-31+G(dp)/SDD). Frequency calculations were conducted to ensure that all optimized geometries correspond to true minima by ensuring the absence of imaginary frequencies. Solvent effects (water) were accounted for through the integral equation formalism polarizable continuum model (IEFPCM)[42] method using the Gaussian 16 default settings. The chosen protocol is consistent with previous works on related cyclometalated compounds.[57–60]

The adiabatic electron affinities (EAs) and ionization potentials (IPs) listed in Table S3† are computed as follows:

$$\mathrm{EA} = E(A_{n+1}) - E(A_n)$$

$$\mathrm{IP} = E(A_{n-1}) - E(A_n)$$

where E stands for absolute energy, A is the molecule under study, and n refers to the total number of electrons. To obtain the adiabatic values, the molecules were minimized for each electronic state by means of the restricted and unrestricted DFT method for closed and open shell systems, respectively. The experimental absorption maxima registered in PBS for systems **1a** and **1b** were used as the S_1 excited-state energy, as summarized in Table S4.† **3c** was optimized with the PBE0/6-31G**/LANL2DZ method in water (COSMO model) as implemented in the GPU-accelerated quantum chemistry code Terachem.[61–63] Dispersion was corrected empirically with Grimme's method using the default Terachem settings.

Cellular take up and accumulation studies

Cell culture and cell lines. HeLa and EO771 cells were cultured in Dulbecco's modified Eagle's medium (DMEM) supplemented with 10% FBS, L-glutamine (2 mM for HeLa and 4 mM for EO771), and 1% penicillin–streptomycin; 20 mM HEPES was added specifically for EO771 cells. Cells were cultured in a humidified incubator at 310 K under a 5% CO_2 atmosphere and subcultured two or three times a week with appropriate densities and confirmed to be mycoplasma-free using a standard Hoechst DNA staining method. A2780cis cells were cultured in RPMI-1640 cell medium supplemented with 10% FBS, L-glutamine (2 mM), and 1% penicillin–streptomycin. Cells were cultured in a humidified incubator at 310 K under a 5% CO_2 atmosphere and subcultured two or three times a week with appropriate densities and confirmed to be mycoplasma-free using a standard Hoechst DNA staining method.

Cellular accumulation by inductively coupled plasma mass spectrometry (ICP-MS). Briefly, A2780cis cells were seeded onto a 12-well plate at a density of 3×10^5 cells per well. Then Ir(III)–COUPY conjugates or Ir(III) complexes were added for 2 h at 10 μM. Cisplatin (10 μM) was included for comparative purposes. Cells were then trypsinized and pelleted for cell counting. Samples were then digested with 30% HNO_3 suprapur acid (Sigma-Aldrich) and measured on an inductively coupled plasma mass spectrometry Agilent 7900 ICP–MS instrument. ^{191}Ir, ^{194}Pt, and ^{195}Pt isotopes were measured. Three independent experiments were performed (n = 2 replicates).

Fluorescence imaging. HeLa Cells were maintained in Dulbecco's modified Eagle's (DMEM) GlutaMAX medium containing high glucose (4.5 g L^{-1}) and supplemented with 10% fetal bovine serum (FBS) and 50 U mL^{-1} penicillin–streptomycin. For cellular take up experiments and subsequent observation under a microscope, cells were seeded on glass-bottomed dishes (P35G-1.5-14-C, MatTek). 24 h after seeding, cells were incubated at 37 °C for 30 min with the corresponding Ir(III)–COUPY conjugate (5 μM) in supplemented DMEM. Then, cells were washed three times with DPBS (Dulbecco's phosphate-buffered saline) to remove excess non-internalized conjugate and maintained in low glucose DMEM without phenol red supplemented with 10 mM HEPES for fluorescence imaging.

For colocalization experiments, HeLa cells were incubated with the corresponding Ir(III)–COUPY conjugate (5 μM) in supplemented DMEM for 30 min at 37 °C. After removing excess conjugate with DPBS, the cells were incubated with WGA (2 μg mL^{-1}) in non-supplemented DMEM for 20 min at 37 °C. LTG (0.2 μM) was added to the medium 5 min before the end of this incubation period. Finally, the cells were washed once more with DPBS and maintained in low glucose DMEM

without phenol red supplemented with 10 mM HEPES for fluorescence imaging.

All microscopy observations were performed using a Zeiss LSM 880 confocal microscope equipped with an argon-ion laser, a 561 nm laser, and a 633 nm laser. The microscope was also equipped with a heating insert (P Lab-Tek S, Pecon). Cells were observed using a 63 × 1.4 oil-immersion objective. Ir(III)–COUPY conjugates **3a–c** were excited using the 561 nm laser and emission was detected from 570 to 660 nm. In colocalization studies, LTG was excited using the 488 nm laser line of the argon-ion laser and detected from 500 to 550 nm, while WGA was excited using the 633 nm laser and detected from 660 to 760 nm. Image analysis was performed using Fiji.[64] All images are colorized using the Fire lookup table from Fiji.[64]

Colocalization analysis. Image analysis was performed using Fiji.[51] For complete WGA and compound signal colocalization at the membrane and vesicle levels, images were processed by median filtering (radius = 1), Gaussian filtering (sigma = 1), and background subtraction (rolling ball radius = 30). Colocalization was then measured using the JaCoP plugin[65] and the Otsu thresholding[66] value.

For colocalization analysis of the signal located in vesicles, images were processed by median filtering (radius = 1), Gaussian filtering (sigma = 1), and background subtraction (rolling ball radius = 10). Then images were segmented using the Otsu thresholding algorithm and the resulting binary images were processed to remove larger and non-circular particles with a size filter between 0 and 1 μm2 and a circularity filter between 0.7 and 1. Processed binary images were converted to 16-bit and multiplied by 257 to obtain images with two grey levels (*i.e.*, 0 and 65535) that finally were used to mask the original 16-bit images. Colocalization was then measured on the masked images using the JaCoP plugin.[65]

Photobiological evaluation

Photocytotoxicity determination. A2780cis and EO771 cells were plated in 96-well plates at a density of 5000 cells per well and maintained in the logarithmic growth phase in complete medium for 24 h at 310 K, 5% CO_2 in a humidified incubator. For hypoxia experiments, hypoxia conditions were set up by the Tissue Culture Service at the University of Murcia using nitrogen (N_2) to displace O_2 down to a minimum of 2% in a Forma Steri-Cycle i160 incubator (Thermo Fisher Scientific). Serial dilutions of the compounds were added at the final concentrations in the range of 0–100 μM in a final volume of 100 μL per well. Light irradiation treatments were performed as follows: 1 h incubation with the compounds in the dark, followed by 1 h incubation under irradiation conditions by placing the LuzChem (Canada) well-plate illuminator fitted with green lamps (1.5 mW cm^{-2} at λ_{max} = 520 nm) or red lamps (15 mW cm^{-2} at λ_{max} = 620 nm) inside the CO_2 incubator. All the cell culture plates subjected to light irradiation included untreated controls to verify that cell viability was not affected by light. Treatment-containing media were then removed, and fresh media were added for a 48 h cell recovery period; the temperature throughout the experiment remained at 310 K. The dark control samples were placed under the same dark conditions and then incubated for 1 h in the dark in the humidified CO_2 incubator. Medium was then aspirated by suction, cells were loaded with 50 μL of MTT solution (1 mg mL^{-1}) for an additional 4 h and then removed, and 50 μL of DMSO was added to solubilize the purple formazan crystals formed in active cells. The absorbance was measured at 570 nm using a microplate reader (FLUOstar Omega), and the IC_{50} values were calculated based on the inhibitory rate curves using the following eqn (6):

$$I = \frac{I_{max}}{1 + \left(\frac{IC_{50}}{C}\right)^{n}} \quad (6)$$

where I represents the percentage inhibition of viability observed, I_{max} is the maximal inhibitory effect, IC_{50} is the concentration that inhibits 50% of maximal growth, C is the concentration of the treatment, and n is the slope of the semi-logarithmic dose–response sigmoidal curve. Non-linear fitting was performed using SigmaPlot 14.0 software. All experiments were performed in three independent studies with n = 3 replicates per concentration level.

ROS photogeneration. ROS levels were determined using the 2′,7′-dichlorofluorescein diacetate (DCFH-DA) probe. A2780cis cells (3×10^5cells per well) were seeded onto 12-well plates for 24 h in a humidified CO_2 incubator under either normoxia (21% O_2) or hypoxia (2% O_2) conditions. Cells were then treated with tested compounds (10 μM) for 1 h. After treatment, cells were washed, trypsinized, collected in Eppendorf tubes and further stained with 10 μM of DCFH-DA for 0.5 h. The samples were then dispatched onto seeded onto 96-well black plates and irradiated with a LED source light from the Luzchem red well plate illuminator (15 mW cm^{-2} at λ_{max} = 620 nm) for 1 h. A Fortessa X20 flow cytometer using the 96 well-plate adaptor enabled cell capture and detection of DCF fluorescence signals on the FL1-H channel (λ_{exc} = 488 nm and λ_{em} = 530 ± 30 nm). Unstained cells served as the blank. Unstained, treated cells were used for subtraction of the basal fluorescence of compounds and to correct fluorescence readings. Stained, untreated cells were used as the control. Three independent experiments were performed with n = 3 replicates.

Characterization of cellular ROS. EO771 cells were seeded on a 12-well plate at a density of 2×10^5 cells per well and incubated for 24 h under normoxia (21% O_2) and hypoxia (2% O_2) conditions in a humidified CO_2 incubator. Then cells were co-treated with 10 μM of the Ir(III)–COUPY conjugates **3a**, **3b**, **3c** and a series of ROS scavengers for 1 h. *N*-Acetylcysteine (NAC, 5 mM) was used as a general radical scavenger. The following scavengers were used for each specific ROS: terephthalic acid (TPA, 20 μM) for hydroxyl radicals ($^{\bullet}OH$); MnTBAP (10 μM) for superoxide anion radicals ($O_2^{\bullet-}$); sodium azide (NaN_3, 5 mM) for singlet oxygen ($^1O_2$); uric acid (100 μM) for peroxynitrite anions ($ONOO^-$); sodium pyruvate (NaPyr, 10 mM) for hydrogen peroxide (H_2O_2). Treatment was followed with 1 h incu-

bation in the dark and then 1 h irradiation with red light. After irradiation, the media were removed and cells were stained with 2′,7′-dichlorofluorescein diacetate (DCFH-DA, 10 μM) for 30 min in the dark. Flow cytometry (Fortessa X20) was performed to detect emission at 530 nm after excitation with a blue laser (488 nm). The assay was carried out for at least three independent experiments (n = 2 per replicate). In a parallel study, A2780cis cells were subjected to the same treatment with Ir(III)–COUPY conjugates but were co-treated only with MnTBAP and NaN_3 to evaluate the potential generation of superoxide anion radicals ($O_2^{\bullet-}$) and singlet oxygen ($^1O_2$), respectively. The results were compared to those obtained in EO771 cells to assess cell-line-dependent differences in ROS generation and photocytoxicity.

Cell death induction. Cell death induction was evaluated using the annexin V-FITC/propidium iodide (AV/PI) dual staining method. Briefly, A2780cis cells (2×10^5 cells per well) were seeded in 12-well plates and incubated overnight at 310 K. Test compounds (10 μM) were added, following the treatment schedule described (1 h incubation + 1 h irradiation with 620 nm light). Irradiated, non-treated cells served as the control group. After 24 h of the drug-free recovery period, cells were harvested by trypsinization, washed with PBS and centrifuged, and the pellets were resuspended in 200 μL of a binding buffer as instructed by the manufacturer (Cayman). The resuspended cell solution was left at room temperature in the dark for 15 min before analysis by flow cytometry (FACSCalibur BecktonDickinson; 10^4 events acquired per sample). Cells were visualized using λ_{exc} = 488 channels and registered at 525 nm and 620 nm for annexin V and propidium iodide in the FL1 and FL2 channels, respectively. Cell populations were classified as follows: AV^-/PI^- (viable cells); AV^-/PI^+ (necrotic cells); AV^+/PI^- and AV^+/PI^+ (apoptotic cells). Alternatively, A2780cis cells were subjected to flow cytometry after PDT treatments to detect morphological changes using FSC and SSC contour plots. Data were analyzed using FlowJo software. Three independent experiments were performed.

Phototherapeutic activity in tumor spheroids

Photocytotoxicity in multicellular tumor spheroids. EO771 multicellular tumor spheroids (MCTS) were generated in 96-well Corning microplates with ultralow attachment surface coating. EO771 cells, at a density of 6×10^3 cells per well, were prepared in complete DMEM and carefully distributed into the designated wells. The plates were then covered and placed in an incubator maintained at 37 °C under a 5% CO_2 atmosphere. Over the course of 3 days, the suspended cells self-assembled into uniform and compact MCTS, each with an average diameter of 400 μm. Initially, the MCTS were treated with Ir(III)–COUPY conjugates at a concentration of 20 μM for 1 h, followed by 1 h of red light irradiation. A control group of spheroids underwent the same treatment but were left in the dark. After treatment, the media were replaced with fresh cell culture medium, and the treatments were repeated every 2 days. Over an 8-day period, the development and characteristics of the MCTS were carefully monitored and changes in volume were analyzed using a DMi1 inverted phase contrast microscope (Leica Microsystems).

Cell death induction in multicellular tumor spheroids. EO771 MCTS were treated with Ir(III)–COUPY conjugates **3a**, **3b**, and **3c** at a concentration of 20 μM for 1 h, followed by 1 h of red light irradiation. After irradiation, the treatment solutions were replaced with fresh cell culture media, and the spheroids were incubated in the dark. This treatment cycle was repeated every two days, followed by two additional days of incubation. Subsequently, the spheroids were stained with calcein AM (2 μM) and propidium iodide (2 μg mL^{-1}) for 30 min at 37 °C under a 5% CO_2 atmosphere. Fluorescence images of the MCTS were captured using a Zeiss Axio Observer 7 inverted fluorescence microscope.

Toxicological *in vivo* study

Animals. Female and male C57BL6/Hsd mice (7 weeks old) were purchased from ENVIGO. All animals were housed in a pathogen-free facility with a 12 h light/dark cycle at constant temperature and humidity, with free access to food and water. The animals were quarantined for 1–2 weeks upon arrival before starting experiments.

Toxicity evaluation. The C57BL6/Hsd mice were randomly divided into four groups, each consisting of three mice, either male (M) or female (F). The groups were designated as Vh-Male, Vh-Female, **3c**-Male, and **3c**-Female.

On day 0, the mice received a single intraperitoneal injection at a volume of 10 mL kg^{-1}. The "Vh" groups, serving as the non-treated control, were administered the vehicle (DMEM culture medium). In contrast, the "**3c**" groups, serving as the treated group, received a solution of compound **3c** in DMEM (5 mg kg^{-1}). Following dose administration, the animals were carefully observed for 7 days and routinely monitored for mortality, morbidity, changes in body weight, and other signs of toxicity related to the treatment.

All animals were sacrificed 7 days post-treatment. Each animal underwent a detailed gross pathological examination, including careful inspection of both external and internal body surfaces, as well as all vital organs. The animals were euthanized using CO_2 asphyxiation, and blood samples (600–800 μL) were collected *via* cardiac puncture in labeled microcentrifuge tubes containing EDTA as an anticoagulant. The samples were then centrifuged for 10 min at 5000 rpm at 4 ± 2 °C to obtain plasma. The plasma samples were then analyzed using a VetScan® comprehensive diagnostic profile reagent rotor with the VetScan VS2 chemistry analyzer (Zoetis). This analysis determined the levels of total proteins, albumin, globulins, total bilirubin, alanine aminotransferase, alkaline phosphatase, amylase, creatinine, glucose, cholesterol, total bile acids, blood urea nitrogen, sodium, potassium, calcium, and phosphorus.

Ethics statement. Animals for this study were housed at the animal facility of the Parc Científic de Barcelona. This facility is registered with the regional competent authority for housing and maintaining animals used in scientific procedures (registration number B-9900044) and with the national competent

authority for the use of genetically modified organisms (notification number A/ES/16/1-03; notification date: 65-7951/2016). All animal experimentation was conducted in accordance with local, national, and European regulations. The procedures were reviewed and approved by the Parc Científic de Barcelona (PCB) Ethical Committee for Animal Experimentation and the Ministry of Agriculture, Livestock, Fisheries, and Food, Government of Catalonia (authorization number AR-9719-P1).

Conclusions

In summary, in this work we achieved potent in-cell PDT effects *via* red-light activated Ir(III)–COUPY conjugates under hypoxic conditions. The incorporation of trifluorobenzyl groups at the cyclometalated ligands of the novel Ir(III)–COUPY photosensitizer **3c** produces an increase in the molar absorption coefficients values in all solvents studied and raises the luminescent quantum yield compared to conjugates **3a** and **3b** (which do not contain such groups). This new conjugate, **3c**, is photostable and triggers type I and type II ROS production under irradiation with red light (>600 nm), as demonstrated by means of spectroscopic methods and EPR and further confirmed by theoretical calculations. Moreover, **3c** exhibits a favorable profile for anticancer PDT since it delivers equipotent photocytotoxicity towards normoxic and hypoxic A2780cis and EO771 cancer cells, with high phototherapeutic indexes (>208) and a hypoxia index close to 1 in both cell lines. Importantly, Ir(III)–COUPY conjugate **3c** was found to be highly phototoxic against EO771 multicellular tumor spheroids under red-light irradiation and showed no signs of toxicity *in vivo*. Taken together, this study demonstrated that the conjugation between COUPY dyes and rationally designed Ir(III) complexes was a strategy at the frontier of the development of new red light-activated photosensitizers capable of operating under hypoxic conditions, showing promise for achieving satisfactory anticancer PDT effects. Similar to our previous results, where we found that small changes to the coumarin scaffold and/or the linker moiety improved the PDT activity of the Ir(III)–COUPY PSs,[29] herein we demonstrated that minimal modifications of the cyclometalated Ir(III) system could also have a profound impact on the resulting conjugate, especially on their hypoxia performance and their dark toxicity. As a result, we conclude that both components of the Ir(III)–COUPY dyad play key roles in conditioning the photobiological properties of the PSs as shown for conjugate **3c**. This opens up new possibilities for designing other Ir(III)–COUPY PSs that operate in the red and near-infrared region of the electromagnetic spectrum with the intent of overcoming the hypoxia limitation.

Author contributions

Conceptualization: E. O.-F., V. M., J. R., S. N. Data curation: E. O.-F., G. V., A. R., P. A., E. I.-G., D. A.-M., M. E. A., A. F.-M. Formal analysis: E. O.-F., P. A., E. I.-G., G. V., M. B., V. M., J. R., S. N., M. E. A., A. F.-M. Funding acquisition: V. M., J. R., S. N., M. E. A., A. F.-M. Investigation: E. O.-F., A. R., P. A., E. I.-G., D. A.-M., G. V., C. H., M. J.-R., A. D., J. G., M. B., M. E. A., A. F.-M. Methodology: E. O.-F., A. R., P. A., E. I.-G., D. A.-M., G. V., C. H., M. J.-R., A. D., J. G., M. B., M. E. A., A. F.-M. Project administration: E. O.-F., G. V., V. M., J. R., S. N., M. E. A., A. F.-M. Resources: V. M., J. R., S. N., J.-L. H., M. E. A., A. F.-M. Software: E. O.-F., G. V., P. A., E. I.-G., M. B., M. E. A., A. F.-M. Supervision: V. M., J. R., S. N. Validation: E. O.-F., A. R., P. A., E. I.-G., D. A.-M., G. V., C. H., M. J.-R., A. D., J. G., M. B., M. E. A., A. F.-M. Writing – original draft: E. O.-F., V. M. Writing – review & editing: E. O.-F., G. V., P. A., E. I.-G., M. B., V. M., J. R., S. N., M. E. A., A. F.-M.

Data availability

The data supporting this article have been included as part of the ESI.†

Conflicts of interest

There are no conflicts to declare.

Acknowledgements

This work was supported by funds from the Spanish Ministerio de Ciencia, Innovación e Universidades and Agencia Estatal de Investigación (MICIU/AEI/10.13039/501100011033) (PID2020-117508RB-I00 and PID2023-146161OB-I00 to V. M.; PID2021-122850NB-I00 to J. R.; PID2021-127554NA-I00 to A. F.-M.; PID2020-115801RB-C22 to S. N.), by "ERDF A way of making Europe". (PID2023-146161OB-I00 to V. M.; PID2021-122850NB-I00 to J. R.; PID2021-127554NA-I00 to A. F.-M.), and Fundación Séneca-CARM (project 21989/PI/22 to J. R.). A. F.-M. is grateful for support from Generalitat Valenciana Project No. CIAICO/2022/121. M. E. A. acknowledges financial support under the PRIN D.D. 104/2022 PNRR M4.C2.1.1. – Project Code: 2022AN47CA – CUP: H53D23003820001, funded by the European Union – NextGenerationEU– Project Title "La-G4-DACA" – Grant Assignment DD 862, 16/06/2023. M. E. A. is also grateful for the CINECA award under the ISCRA initiative, for the availability of high-performance computing resources and support (IsCc4_PAC-DACA project). E. O-F. thanks AECC (Project PRDMU19003ORTE). E. O.-F. was supported by JDC2023-050936-I funded by MICIU/AEI/10.13039/501100011033 and FSE+. A. R. was a recipient of a fellowship from the University of Barcelona (APIF). C. H. thanks the SUR del DEC de la Generalitat de Catalunya and the FSE for his predoctoral fellowship (Grants No. 2017 FI_B_00617, 2018 FI_B1 00174 and 2019 FI_B2 00167). E. I.-G. acknowledges support from a Margarita Salas postdoctoral grant at the University of Barcelona, funded by the Spanish Ministerio de Universidades with European Union funds – NextGenerationEU. S. N. thanks

the Departament de Recerca i Universitats de la Generalitat de Catalunya for the support given to his research group (2021 SGR 01023) and the ICREA-Catalan Institution for Research and Advanced Studies for grant no. Ac2232308. The valuable collaboration of the technicians from the NMR, HRMS, ICP-MS, confocal microscopy and EPR facilities of the Scientific and Technological Centers (CCiTUB) of the Universitat de Barcelona is also appreciated.

References

1 X. Wang, J. Peng, C. Meng and F. Feng, Recent advances for enhanced photodynamic therapy: from new mechanisms to innovative strategies, *Chem. Sci.*, 2024, **15**, 12234–12257.
2 W. Jiang, M. Liang, Q. Lei, G. Li and S. Wu, The Current Status of Photodynamic Therapy in Cancer Treatment, *Cancers*, 2023, **15**, 585.
3 G. Li, Q. Wang, J. Liu, M. Wu, H. Ji, Y. Qin, X. Zhou and L. Wu, Innovative strategies for enhanced tumor photodynamic therapy, *J. Mater. Chem. B*, 2021, **9**, 7347–7370.
4 T. C. Pham, V.-N. Nguyen, Y. Choi, S. Lee and J. Yoon, Recent Strategies to Develop Innovative Photosensitizers for Enhanced Photodynamic Therapy, *Chem. Rev.*, 2021, **121**, 13454–13619.
5 X. Zhao, J. Liu, J. Fan, H. Chao and X. Peng, Recent progress in photosensitizers for overcoming the challenges of photodynamic therapy: from molecular design to application, *Chem. Soc. Rev.*, 2021, **50**, 4185–4219.
6 E. Ortega-Forte, A. Rovira, A. Gandioso, J. Bonelli, M. Bosch, J. Ruiz and V. Marchán, COUPY Coumarins as Novel Mitochondria-Targeted Photodynamic Therapy Anticancer Agents, *J. Med. Chem.*, 2021, **64**, 17209–17220.
7 J. Bonelli, E. Ortega-Forte, A. Rovira, M. Bosch, O. Torres, C. Cuscó, J. Rocas, J. Ruiz and V. Marchán, Improving Photodynamic Therapy Anticancer Activity of a Mitochondria-Targeted Coumarin Photosensitizer Using a Polyurethane-Polyurea Hybrid Nanocarrier, *Biomacromolecules*, 2022, **23**, 2900–2913.
8 Y. Wen, W. Zhang, N. Gong, Y.-F. Wang, H.-B. Guo, W. Guo, P. C. Wang and X.-J. Liang, Carrier-free, self-assembled pure drug nanorods composed of 10-hydroxycamptothecin and chlorin e6 for combinatorial chemo-photodynamic antitumor therapy *in vivo*, *Nanoscale*, 2017, **9**, 14347–14356.
9 A. Escudero, C. Carrillo-Carrión, M. C. Castillejos, E. Romero-Ben, C. Rosales-Barrios and N. Khiar, Photodynamic therapy: photosensitizers and nanostructures, *Mater. Chem. Front.*, 2021, **5**, 3788–3812.
10 L. M. Lifshits, J. A. R. Iii, P. Konda, S. Monro, H. D. Cole, D. von Dohlen, S. Kim, G. Deep, R. P. Thummel, C. G. Cameron, S. Gujar and S. A. McFarland, Near-infrared absorbing Ru(II) complexes act as immunoprotective photodynamic therapy (PDT) agents against aggressive melanoma, *Chem. Sci.*, 2020, **11**, 11740–11762.
11 R. Bevernaegie, B. Doix, E. Bastien, A. Diman, A. Decottignies, O. Feron and B. Elias, Exploring the Phototoxicity of Hypoxic Active Iridium(III)-Based Sensitizers in 3D Tumor Spheroids, *J. Am. Chem. Soc.*, 2019, **141**, 18486–18491.
12 F. J. Ballester, E. Ortega, D. Bautista, M. D. Santana and J. Ruiz, Ru(ii) photosensitizers competent for hypoxic cancers via green light activation, *Chem. Commun.*, 2020, **56**, 10301–10304.
13 J. Pracharova, G. Vigueras, V. Novohradsky, N. Cutillas, C. Janiak, H. Kostrhunova, J. Kasparkova, J. Ruiz and V. Brabec, Exploring the Effect of Polypyridyl Ligands on the Anticancer Activity of Phosphorescent Iridium(III) Complexes: From Proteosynthesis Inhibitors to Photodynamic Therapy Agents, *Chem. – Eur. J.*, 2018, **24**, 4607–4619.
14 L. Lilge, M. Roufaiel, S. Lazic, P. Kaspler, M. A. Munegowda, M. Nitz, J. Bassan and A. Mandel, Evaluation of a Ruthenium coordination complex as photosensitizer for PDT of bladder cancer: Cellular response, tissue selectivity and *in vivo* response, *Transl. Biophotonics*, 2020, **2**, e201900032.
15 L. C.-C. Lee, K.-K. Leung and K. K.-W. Lo, Recent development of luminescent rhenium(I) tricarbonyl polypyridine complexes as cellular imaging reagents, anticancer drugs, and antibacterial agents, *Dalton Trans.*, 2017, **46**, 16357–16380.
16 C. Imberti, P. Zhang, H. Huang and P. J. Sadler, New Designs for Phototherapeutic Transition Metal Complexes, *Angew. Chem., Int. Ed.*, 2020, **59**, 61–73.
17 Y. Zhang, B.-T. Doan and G. Gasser, Metal-Based Photosensitizers as Inducers of Regulated Cell Death Mechanisms, *Chem. Rev.*, 2023, **123**, 10135–10155.
18 Y. Wu, S. Li, Y. Chen, W. He and Z. Guo, Recent advances in noble metal complex based photodynamic therapy, *Chem. Sci.*, 2022, **13**, 5085–5106.
19 L. Qiao, J. Liu, S. Kuang, X. Liao, J. Kou, L. Ji and H. Chao, A mitochondrion-targeted BODIPY-Ir(III) conjugate as a photoinduced ROS generator for the oxidative destruction of triple-negative breast cancer cells, *Dalton Trans.*, 2021, **50**, 14332–14341.
20 B. Liu, S. Monro, M. A. Jabed, C. G. Cameron, K. L. Colón, W. Xu, S. Kilina, S. A. McFarland and W. Sun, Neutral iridium(III) complexes bearing BODIPY-substituted N-heterocyclic carbene (NHC) ligands: synthesis, photophysics, in vitro theranostic photodynamic therapy, and antimicrobial activity, *Photochem. Photobiol. Sci.*, 2019, **18**, 2381–2396.
21 L. Zhang, Y. Geng, L. Li, X. Tong, S. Liu, X. Liu, Z. Su, Z. Xie, D. Zhu and M. R. Bryce, Rational design of iridium–porphyrin conjugates for novel synergistic photodynamic and photothermal therapy anticancer agents, *Chem. Sci.*, 2021, **12**, 5918–5925.
22 Y. Wu, J. Wu and W.-Y. Wong, *Biomater. Sci.*, 2021, **9**, 4843–4853.
23 C. Liu, L. Zhou, F. Wei, L. Li, S. Zhao, P. Gong, L. Cai and K. M.-C. Wong, Versatile Strategy To Generate a Rhodamine Triplet State as Mitochondria-Targeting Visible-Light

Photosensitizers for Efficient Photodynamic Therapy, *ACS Appl. Mater. Interfaces*, 2019, **11**, 8797–8806.

24 K.-X. Teng, W.-K. Chen, L.-Y. Niu, W.-H. Fang, G. Cui and Q.-Z. Yang, BODIPY-Based Photodynamic Agents for Exclusively Generating Superoxide Radical over Singlet Oxygen, *Angew. Chem., Int. Ed.*, 2021, **60**, 19912–19920.

25 B. Lu, L. Wang, H. Tang and D. Cao, Recent advances in type I organic photosensitizers for efficient photodynamic therapy for overcoming tumor hypoxia, *J. Mater. Chem. B*, 2023, **11**, 4600–4618.

26 J. An, S. Tang, G. Hong, W. Chen, M. Chen, J. Song, Z. Li, X. Peng, F. Song and W.-H. Zheng, An unexpected strategy to alleviate hypoxia limitation of photodynamic therapy by biotinylation of photosensitizers, *Nat. Commun.*, 2022, **13**, 2225.

27 V. Novohradsky, A. Rovira, C. Hally, A. Galindo, G. Vigueras, A. Gandioso, M. Svitelova, R. Bresolí-Obach, H. Kostrhunova, L. Markova, J. Kasparkova, S. Nonell, J. Ruiz, V. Brabec and V. Marchán, Towards Novel Photodynamic Anticancer Agents Generating Superoxide Anion Radicals: A Cyclometalated IrIII Complex Conjugated to a Far-Red Emitting Coumarin, *Angew. Chem., Int. Ed.*, 2019, **58**, 6311–6315.

28 V. Novohradsky, L. Markova, H. Kostrhunova, J. Kasparkova, J. Ruiz, V. Marchán and V. Brabec, A Cyclometalated IrIII Complex Conjugated to a Coumarin Derivative Is a Potent Photodynamic Agent against Prostate Differentiated and Tumorigenic Cancer Stem Cells, *Chem. – Eur. J.*, 2021, **27**, 8547–8556.

29 A. Rovira, E. Ortega-Forte, C. Hally, M. Jordà-Redondo, D. Abad-Montero, G. Vigueras, J. I. Martínez, M. Bosch, S. Nonell, J. Ruiz and V. Marchán, Exploring Structure–Activity Relationships in Photodynamic Therapy Anticancer Agents Based on Ir(III)-COUPY Conjugates, *J. Med. Chem.*, 2023, **66**, 7849–7867.

30 E. Ortega-Forte, A. Rovira, M. López-Corrales, A. Hernández-García, F. J. Ballester, E. Izquierdo-García, M. Jordà-Redondo, M. Bosch, S. Nonell, M. D. Santana, J. Ruiz, V. Marchán and G. Gasser, A near-infrared light-activatable Ru(II)-coumarin photosensitizer active under hypoxic conditions, *Chem. Sci.*, 2023, **14**, 7170–7184.

31 G. Vigueras, L. Markova, V. Novohradsky, A. Marco, N. Cutillas, H. Kostrhunova, J. Kasparkova, J. Ruiz and V. Brabec, A photoactivated Ir(III) complex targets cancer stem cells and induces secretion of damage-associated molecular patterns in melanoma cells characteristic of immunogenic cell death, *Inorg. Chem. Front.*, 2021, **8**, 4696–4711.

32 V. Novohradsky, G. Vigueras, J. Pracharova, N. Cutillas, C. Janiak, H. Kostrhunova, V. Brabec, J. Ruiz and J. Kasparkova, Molecular superoxide radical photogeneration in cancer cells by dipyridophenazine iridium(III) complexes, *Inorg. Chem. Front.*, 2019, **6**, 2500–2513.

33 L. Wang, J. Karges, F. Wei, L. Xie, Z. Chen, G. Gasser, L. Ji and H. Chao, A mitochondria-localized iridium(III) photosensitizer for two-photon photodynamic immunotherapy against melanoma, *Chem. Sci.*, 2023, **14**, 1461–1471.

34 B. Liu, S. Monro, Z. Li, M. A. Jabed, D. Ramirez, C. G. Cameron, K. Colón, J. I. Roque, S. Kilina, J. Tian, S. A. McFarland and W. Sun, New Class of Homoleptic and Heteroleptic Bis(terpyridine) Iridium(III) Complexes with Strong Photodynamic Therapy Effects, *ACS Appl. Bio Mater.*, 2019, **2**, 2964–2977.

35 H. Huang, S. Banerjee, K. Qiu, P. Zhang, O. Blacque, T. Malcomson, M. J. Paterson, G. J. Clarkson, M. Staniforth, V. G. Stavros, G. Gasser, H. Chao and P. J. Sadler, Targeted photoredox catalysis in cancer cells, *Nat. Chem.*, 2019, **11**, 1041–1048.

36 C. Huang, C. Liang, T. Sadhukhan, S. Banerjee, Z. Fan, T. Li, Z. Zhu, P. Zhang, K. Raghavachari and H. Huang, *In vitro* and *In vivo* Photocatalytic Cancer Therapy with Biocompatible Iridium(III) Photocatalysts, *Angew. Chem.*, 2021, **133**, 9560–9565.

37 J. Yellol, S. A. Pérez, G. Yellol, J. Zajac, A. Donaire, G. Vigueras, V. Novohradsky, C. Janiak, V. Brabec and J. Ruiz, Highly potent extranuclear-targeted luminescent iridium(III) antitumor agents containing benzimidazole-based ligands with a handle for functionalization, *Chem. Commun.*, 2016, **52**, 14165–14168.

38 C. Adamo and V. Barone, Toward reliable density functional methods without adjustable parameters: The PBE0 model, *J. Chem. Phys.*, 1999, **110**, 6158–6170.

39 S. Grimme, J. Antony, S. Ehrlich and H. Krieg, A consistent and accurate ab initio parametrization of density functional dispersion correction (DFT-D) for the 94 elements H-Pu, *J. Chem. Phys.*, 2010, **132**, 154104.

40 M. J. Frisch, G. W. Trucks, H. B. Schlegel, G. E. Scuseria, M. A. Robb, J. R. Cheeseman, G. Scalmani, V. Barone, G. A. Petersson, H. Nakatsuji, X. Li, M. Caricato, A. V. Marenich, J. Bloino, B. G. Janesko, R. Gomperts, B. Mennucci, H. P. Hratchian, J. V. Ortiz, A. F. Izmaylov, J. L. Sonnenberg, D. Williams-Young, F. Ding, F. Lipparini, F. Egidi, J. Goings, B. Peng, A. Petrone, T. Henderson, D. Ranasinghe, V. G. Zakrzewski, J. Gao, N. Rega, G. Zheng, W. Liang, M. Hada, M. Ehara, K. Toyota, R. Fukuda, J. Hasegawa, M. Ishida, T. Nakajima, Y. Honda, O. Kitao, H. Nakai, T. Vreven, K. Throssell, J. A. Montgomery Jr., J. E. Peralta, F. Ogliaro, M. J. Bearpark, J. J. Heyd, E. N. Brothers, K. N. Kudin, V. N. Staroverov, T. A. Keith, R. Kobayashi, J. Normand, K. Raghavachari, A. P. Rendell, J. C. Burant, S. S. Iyengar, J. Tomasi, M. Cossi, J. M. Millam, M. Klene, C. Adamo, R. Cammi, J. W. Ochterski, R. L. Martin, K. Morokuma, O. Farkas, J. B. Foresman and D. J. Fox, *Gaussian 16*, Gaussian, Inc., Wallingford, CT, 2016.

41 D. Andrae, U. Häußermann, M. Dolg, H. Stoll and H. Preuß, Energy-Adjusted ab initio Pseudopotentials for the Second and Third Row Transition Elements, *Theor. Chim. Acta*, 1990, **77**, 123–141.

42 J. Tomasi, B. Mennucci and R. Cammi, Quantum Mechanical Continuum Solvation Models, *Chem. Rev.*, 2005, **105**, 2999–3093.

43 R. U. Kadam, D. Garg, J. Schwartz, R. Visini, M. Sattler, A. Stocker, T. Darbre and J.-L. Reymond, CH-π "T-Shape"

Interaction with Histidine Explains Binding of Aromatic Galactosides to Pseudomonas aeruginosa Lectin LecA, *ACS Chem. Biol.*, 2013, **8**, 1925–1930.

44 S. Bolte and F. P. Cordelières, A guided tour into subcellular colocalization analysis in light microscopy, *J. Microsc.*, 2006, **224**, 213–232.

45 B. C. Behrens, T. C. Hamilton, H. Masuda, K. R. Grotzinger, J. Whang-Peng, K. G. Louie, T. Knutsen, W. M. McKoy, R. C. Young and R. F. Ozols, Characterization of a cis-Diamminedichloroplatinum(II)-resistant Human Ovarian Cancer Cell Line and Its Use in Evaluation of Platinum Analogues, *Cancer Res.*, 1987, **47**, 414–418.

46 D. Fink, S. Aebi and S. B. Howell, The role of DNA mismatch repair in drug resistance, *Clin. Cancer Res.*, 1998, **4**, 1–6.

47 M. Li, Y. Xu, Z. Pu, T. Xiong, H. Huang, S. Long, S. Son, L. Yu, N. Singh, Y. Tong, J. L. Sessler, X. Peng and J. S. Kim, Photoredox catalysis may be a general mechanism in photodynamic therapy, *Proc. Natl. Acad. Sci. U. S. A.*, 2022, **119**, e2210504119.

48 C. Huang, C. Liang, T. Sadhukhan, S. Banerjee, Z. Fan, T. Li, Z. Zhu, P. Zhang, K. Raghavachari and H. Huang, *In vitro* and *In vivo* Photocatalytic Cancer Therapy with Biocompatible Iridium(III) Photocatalysts, *Angew. Chem., Int. Ed.*, 2021, **60**, 9474–9479.

49 T. Fan, J. Song and L.-Z. Gong, Asymmetric Redox Allylic Alkylation to Access 3,3′-Disubstituted Oxindoles Enabled by Ni/NHC Cooperative Catalysis, *Angew. Chem., Int. Ed.*, 2022, **61**, e202201678.

50 T. Wei, W. Liu, S. Zhang, Q. Liu, J. Luo and X. Liu, A dual-functional Bi-doped Co_3O_4 nanosheet array towards high efficiency 5-hydroxymethylfurfural oxidation and hydrogen production, *Chem. Commun.*, 2023, **59**, 442–445.

51 S. J. Han, S. Kwon and K. S. Kim, Challenges of applying multicellular tumor spheroids in preclinical phase, *Cancer Cell Int.*, 2021, **21**, 152.

52 D. Magde, J. H. Brannon, T. L. Cremers and J. Olmsted, Absolute luminescence yield of cresyl violet. A standard for the red, *J. Phys. Chem.*, 1979, **83**, 696–699.

53 C. Würth, M. Grabolle, J. Pauli, M. Spieles and U. Resch-Genger, Relative and absolute determination of fluorescence quantum yields of transparent samples, *Nat. Protoc.*, 2013, **8**, 1535–1550.

54 A. M. Brouwer, Standards for photoluminescence quantum yield measurements in solution (IUPAC Technical Report), *Pure Appl. Chem.*, 2011, **83**, 2213–2228.

55 P. G. Seybold and M. Gouterman, Porphyrins: XIII: Fluorescence spectra and quantum yields, *J. Mol. Spectrosc.*, 1969, **31**, 1–13.

56 Y. Han, X. Liu, Z. Tian, X. Ge, J. Li, M. Gao, Y. Li, Y. Liu and Z. Liu, Half-sandwich Iridium(III) Benzimidazole-Appended Imidazolium-Based N-heterocyclic Carbene Complexes and Antitumor Application, *Chem. – Asian J.*, 2018, **13**, 3697–3705.

57 J. A. Roque III, H. Cole, P. Barrett, L. Lifshits, R. Hodges, S. Kim, A. Francés-Monerris, M. E. Alberto, C. Cameron and S. McFarland, Intraligand Excited States Turn a Ruthenium Oligothiophene Complex into a Light-Triggered Ubertoxin with Anticancer Effects in Extreme Hypoxia, *J. Am. Chem. Soc.*, 2022, **144**, 8317–8336.

58 H. D. Cole, A. Vali, J. A. Roque III, G. Shi, G. Kaur, R. O. Hodges, A. Francés-Monerris, M. E. Alberto, C. G. Cameron and S. A. McFarland, Ru(II) Phenanthroline-Based Oligothienyl Complexes as Phototherapy Agents, *Inorg. Chem.*, 2023, **62**, 21181–21200.

59 H. D. Cole, A. Vali, J. A. Roque III, G. Shi, A. Talgatov, G. Kaur, A. Francés-Monerris, M. E. Alberto, C. G. Cameron and S. A. McFarland, Ru(II) Oligothienyl Complexes with Fluorinated Ligands: Photophysical, Electrochemical, and Photobiological Properties, *Inorg. Chem.*, 2024, **63**, 9735–9752.

60 J. A. Roque, P. C. Barrett, H. D. Cole, L. M. Lifshits, G. Shi, S. Monro, D. von Dohlen, S. Kim, N. Russo, G. Deep, C. G. Cameron, M. E. Alberto and S. A. McFarland, Breaking the barrier: an osmium photosensitizer with unprecedented hypoxic phototoxicity for real world photodynamic therapy, *Chem. Sci.*, 2020, **11**, 9784–9806.

61 I. S. Ufimtsev and T. J. Martínez, Quantum Chemistry on Graphical Processing Units. 1. Strategies for Two-Electron Integral Evaluation, *J. Chem. Theory Comput.*, 2008, **4**, 222–231.

62 I. S. Ufimtsev and T. J. Martinez, Quantum Chemistry on Graphical Processing Units. 2. Direct Self-Consistent-Field Implementation, *J. Chem. Theory Comput.*, 2009, **5**, 1004–1015.

63 I. S. Ufimtsev and T. J. Martinez, Quantum Chemistry on Graphical Processing Units. 3. Analytical Energy Gradients, Geometry Optimization, and First Principles Molecular Dynamics, *J. Chem. Theory Comput.*, 2009, **5**, 2619–2628.

64 J. Schindelin, I. Arganda-Carreras, E. Frise, V. Kaynig, M. Longair, T. Pietzsch, S. Preibisch, C. Rueden, S. Saalfeld, B. Schmid, J.-Y. Tinevez, D. J. White, V. Hartenstein, K. Eliceiri, P. Tomancak and A. Cardona, Fiji: an open-source platform for biological-image analysis, *Nat. Methods*, 2012, **9**, 676–682.

65 S. Bolte and F. P. Cordelières, A guided tour into subcellular colocalization analysis in light microscopy, *J. Microsc.*, 2006, **224**, 213–232.

66 N. Otsu, A threshold selection method from gray-level histograms, *IEEE Trans. Syst., Man, Cybern.*, 1979, **9**, 62–66.